

1 Sardinia Radio Telescope structural behavior under solar thermal load

2 **Alessandro Attoli**

3 *alessandro.attoli@inaf.it, INAF–OAC Osservatorio Astronomico di Cagliari, Selargius, Italy*

4

5 **Flavio Stochino***

6 *Corresponding Author: fstochino@unica.it, DICAAR, Università degli Studi di Cagliari, via Marengo 2,*

7 *09123 Cagliari, Italy*

8

9 **Franco Buffa**

10 *franco.buffa@inaf.it, INAF–OAC Osservatorio Astronomico di Cagliari, Selargius, Italy*

11

12 **Sergio Poppi**

13 *sergio.poppi@inaf.it, INAF–OAC Osservatorio Astronomico di Cagliari, Selargius, Italy*

14

15 **Giampaolo Serra**

16 *giampaolo.serra@asi.it, Agenzia Spaziale Italiana (ASI), CSG-Unità Capo Sito Sardegna, Sede ASI-Cagliari,*

17 *presso INAF–OAC Osservatorio Astronomico di Cagliari, Selargius, Italy*

18

19 **Giannina Sanna**

20 *topoca@unica.it, DICAAR, Università degli Studi di Cagliari, via Marengo 2, 09123 Cagliari, Italy*

21 **Antonio Cazzani**

22 *antonio.cazzani@unica.it, DICAAR, Università degli Studi di Cagliari, via Marengo 2, 09123 Cagliari, Italy*

23

24 Abstract

25 Sardinia Radio Telescope (SRT) with its 64m diameter primary mirror is a modern radio-astronomic facility.

26 Its large dimensions allow to reach high performances, but, at the same time, make the antenna sensitive to

27 deformations caused by environmental factors such as gravity, wind and temperature changes. Indeed, it is

28 important to determine the effects that environmental loads produce on this structure. In this paper, the SRT

29 pointing error variation produced by solar radiation acting on its structural system has been studied. Through

30 a sensitivity analysis it was possible to establish that the Alidade is the radio telescope component that produces

31 higher pointing errors when subjected to thermal load. Then, an analytical model was used to estimate the

32 temperature of the Alidade trusses exposed to solar radiation. Furthermore, the calibration of the analytical

33 model parameters was performed by comparing the experimental data obtained by thermographic

34 investigations. Then, using Finite Element Analysis, the pointing error generated by each simulated thermal
35 scenario was determined. Finally, the numerical results allow to better understand the structural behavior of
36 SRT in realistic thermal conditions.

37

38 1. Introduction

39 Protected from urban electromagnetic interference, not too far from Cagliari (Italy), the Sardinia Radio
40 Telescope (SRT – www.srt.inaf.it) scans the sky. With its 64m diameter primary mirror, SRT is a modern
41 radio-astronomic facility. It has a Gregorian configuration, with a shaped primary mirror (M1) and an elliptical
42 shaped secondary mirror (M2). The main mirror is characterized by an active surface made up of panels that
43 can be oriented by means of electromechanical actuators, (Bolli et al., 2015), (Stochino et al., 2017), (Buffa et
44 al., 2017). SRT has been designed to work inside a frequency band between 300MHz and 116GHz (wavelength
45 range between 1000 mm and 3 mm).

46 Its large aperture allows to reach high antenna gain and formidable angular resolution. Generally, this kind of
47 antenna has the best performances in small elevation angular ranges around the elevation at which its
48 mechanical alignment has been done (at 45 ° in the case of SRT). At other angular elevations, i.e. varying the
49 pointing direction of the antenna, the performances get worse, if not compensated, decreasing the gain and the
50 pointing accuracy. This is due to the gravitational loads, which mainly change the profile of the main reflector
51 surface and modify the alignment between main and sub-reflectors, to the thermal load and to the wind
52 pressure, which can deform the beam structure (alidade) supporting the reflectors and modify the main
53 reflectors positions. The SRT active optics can compensate the main reflector deformations and the reflectors
54 axis alignment by dedicated look-up tables coming from photogrammetry and laser tracker combined
55 measurements (Süss et al., 2012) (Baars, 2007). Instead, the effect of the thermal loads and the wind on the
56 SRT pointing accuracy needs a deep investigation, now more than ever, considering that the antenna is about
57 to be upgraded with higher frequency receivers which will allow to extend the maximum operative frequency
58 from 26.5 GHz (required pointing accuracy 4.4 arcsec) to 116 GHz (required pointing accuracy 1 arcsec)
59 (Govoni et al., 2021).

60 Therefore, it would be important to optimize the position of thermal sensors after a sensitivity study on what
61 are the most SRT parts that mostly influence the pointing error due to thermal deformations.

62 In literature, the non-uniform thermal load has been analyzed for many complex three-dimensional structures
63 (Chen et al., 2020), (Chen et al., 2021) considering also the fatigue effects caused by cyclic thermal loads
64 (Wang et al., 2021).

65 If we focus on telescopes, the great influence of the alidade on pointing error has been already highlighted in
66 many cases. In (Fu et al., 2016) the effects on pointing accuracy due to real temperature field distributions on
67 the TM65m antenna alidade were analyzed; thermal deformations were computed from measures taken by
68 inclinometers. (Ambrosini et al., 2016) describes how the thermal behavior of the of the 32 meter VLBI
69 parabola at Medicina was studied, through the data collected with thermal sensors distributed on the alidade
70 and an inclinometer positioned in the axis of elevation.

71 How to use inclinometer information for monitoring the rail and the thermal gradient effects on the SRT
72 Alidade structure is presented in (Pisanu et al., 2014). (Ukita et al., 2007) also propose a study of the effects
73 that thermal loads together with wind action produce on the ASTE 10-m Antenna.

74 In order to determine the thermal load due to solar radiation it is possible to use a numerical approach, based
75 on computational fluid dynamics (Drozdol, 2021), (Losi et al., 2021), or to develop an experimental campaign
76 measuring real temperatures on site (Li et al., 2021). In the latter paper the problem is treated through an
77 approach based on Finite Element (FE) method integrated with field measurements that allow to develop a
78 model updating capable of reaching good accuracy. An example is proposed in (Zhao et al., 2019) in which
79 the FE method is used to study of the effects on the pointing of radio telescopes caused by gravity, thermal
80 gradients, and wind disturbances. In (Greve et al., 2005), temperature measurements are applied to finite
81 element model in order to calculate structural deformation of the Institut de Radioastronomie Millimétrique
82 30-m telescope.

83 (Stochino et al., 2015) describe a method for updating a finite element model of the Sardinia Radio Telescope
84 in order to more accurately estimate the displacements of the structure caused by gravity and thermal loads.

85 The latter approach uses the photogrammetric survey as the only benchmark. (Buffa et al., 2015) presents the

86 results of Finite Element analyses to make a comparison with the experimental data deriving from
87 photogrammetric investigations.

88 The evaluation of the correlation of antennas pointing error and solar thermal load is a current research topic
89 that requires further investigations. In addition, given that SRT will be upgraded soon with higher frequency
90 receivers the accurate evaluation of thermal loads effects is of paramount relevance. Thus, this paper
91 investigates the antenna pointing error produced by solar radiation, taking into account possible phenomena of
92 differentiated irradiation due to shading and exposure using innovative analytical and numerical models.

93 After this brief introduction, in Section 2, a sensitivity analysis is proposed to identify the components of the
94 telescope that most influence pointing under thermal load. The study of the effects on pointing generated by a
95 uniform thermal load scenario is described in Section 3. Section 4 is dedicated to the presentation of an
96 analytical model for estimating the temperature of a surface subjected to solar radiation. A methodology to
97 estimate radiation using commercial software is presented in Section 5. Section 6 proposes a method to
98 calibrate, through thermographic investigations, the parameters that modify heat balance. The numerical
99 results of the Finite Element Analyses (FEA) are described in Section 7. Finally, concluding remarks and future
100 developments are drawn in Section 8.

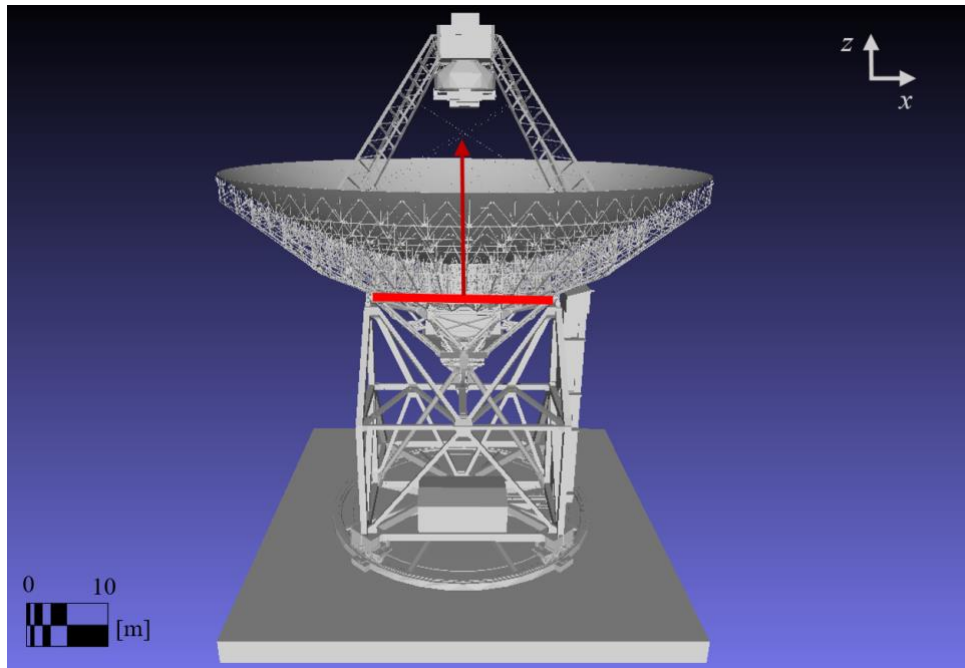
101

102 2. Pointing error sensitivity analysis

103 At first, it is necessary to define a parameter that clearly indicates the direction observed by Sardinia Radio
104 Telescope when it receives the signal from a source in the sky. At the same time, this parameter must provide
105 information on the accuracy of the observations and on possible pointing errors.

106 For this reason, an ideal vector located in the intersection between azimuth and elevation axes (Figure 1),
107 which in the absence of any load has an ideal direction, represents the reference parameter for estimating the
108 pointing error. For the sake of clarity: the elevation angle is equal to zero when the pointing vector lies on a
109 horizontal plane and it is equal to 90° when the pointing vector coincides with the alidade rotation axis.

110



111

112 *Figure 1: Theoretical pointing vector of SRT when the antenna is at an elevation angle of 90 °.*

113 This vector direction changes with the variation of the parabola elevation and the alidade rotation around the
 114 vertical axis. The definition of the pointing vector does not consider the effects of M2 positioned in the
 115 quadrupod peak. In fact, M2 is considered to be always aligned through the action of six actuators. The position
 116 is defined by means of a look-up table based on metrological measurements. At this moment, thermal loads
 117 are not considered and the current corrections are based only on a parametric pointing model.

118 Due to external actions, the SRT pointing vector undergoes rotations and translations with respect to its ideal
 119 position. However, given that the observed objects are located at infinite distance from the observer, the
 120 translations don't affect the pointing error. Instead, small rotations can lead to large errors in pointing an
 121 astronomical target. In order to identify which components of the radio telescope have the greatest influence
 122 on focus pointing when subjected to thermal stress, a sensitivity analysis was performed using a finite element
 123 model of SRT developed in ANSYS environment (Stolarski et al., 2018).

124 The ANSYS finite element (FE) model of the antenna is composed of 93,635 elements and 92,788 nodes; the
 125 presented composition of the 3D system produced a total amount of degrees of freedom equal to 463,871
 126 (Figure 2).

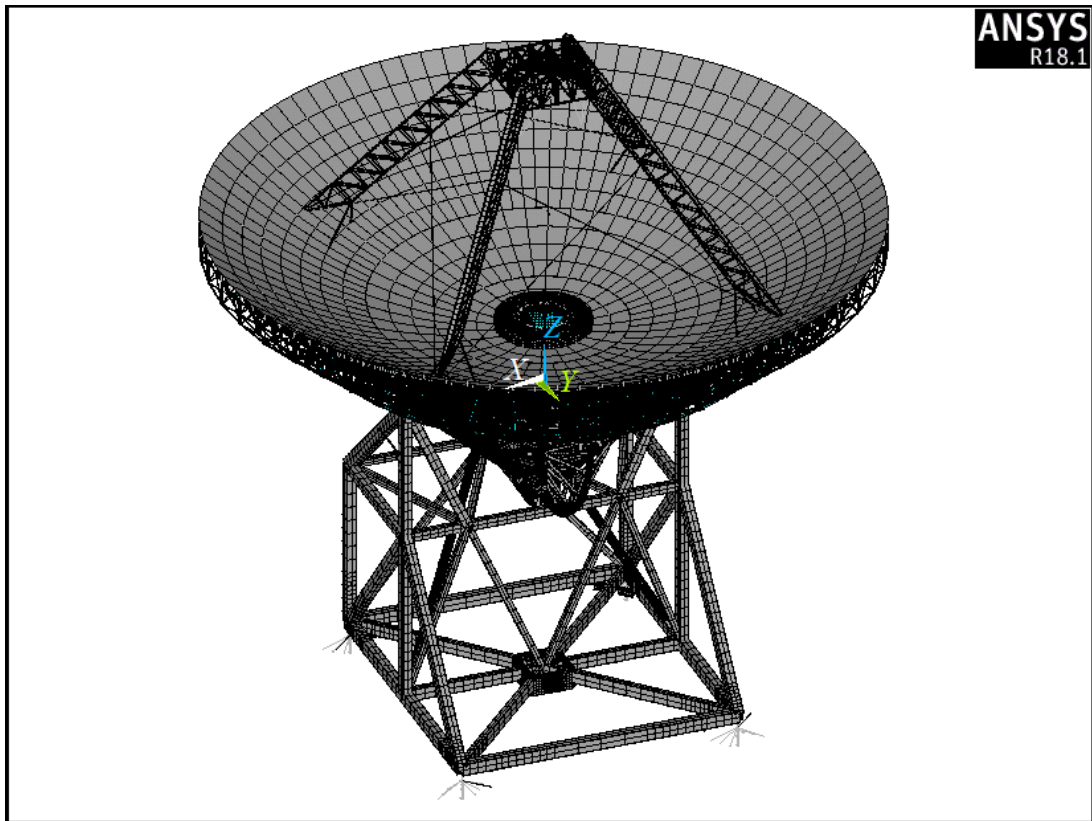


Figure 2: Finite Element Model of the Sardinia Radio Telescope at an elevation angle of 90° .

The cartesian reference axes x, y, z are presented in Figure 2, while the rotation axis points the rotations around the azimuth or vertical direction (that coincides with z axis in Figure 2) and the elevation axis define the rotations in the plane containing the azimuth and the horizontal direction.

The parts that can be recognized in the described model are listed in the following bottom-up sequence:

- *Reinforced concrete base and foundation rail*: although they have not been modelled, they are considered through appropriate constraints at the base to ensure the verticality of the azimuth axis;
- *Alidade*: structural frame that supports all the moving components that can tilt around the elevation axis; it is modelled using both two-noded Timoshenko beam elements with seven degrees of freedom per node (linear translations along the x, y, z direction, rotations around the x, y, z axis, and warping), and two-noded beam elements with six degrees of freedom per node (linear translations along the x, y, z direction and rotations around the x, y, z axis).
- *Back Up Structure (BUS)*: Truss structure which supports the primary mirror, connected to the alidade through the cradle containing the elevation axis; it is modelled by assembling two-noded beam elements

142 with six degrees of freedom per node (linear translations along the x , y , z direction and rotations around
143 the x , y , z axis) in order to obtain a refined 3D system.

- 144 • *Primary Mirror (M1)*: active surface with a diameter of 64m composed of 1008 aluminium panels which
145 can be moved by 1116 electromechanical actuators; Each panel is modelled by means of a four-noded
146 shell element with six degrees of freedom per node (linear translations along the x , y , z direction and
147 rotations around the x , y , z axis) and it is connected to the BUS by means of rigid multi-point-constraint
148 element.
- 149 • *Quadrupod structure*: four legs truss structure that support the Secondary Mirror (M2) and the Prime Focus
150 Positioner (PFP) which hosts some receivers; it is modelled using two-noded Timoshenko beam elements
151 and four-noded shell elements; both have six degrees of freedom per node (linear translations along the x ,
152 y , z direction and rotations around the x , y , z axis).
- 153 • *Secondary Mirror (M2)*: secondary reflector positioned on the top of the Quadrupod structure. Only the
154 support structures of the component were modeled, through multi-point-constraint elements; lumped mass
155 elements complete the representation of M2.

156 The reason for this choice is simple and can be explained shortly. Indeed, the Alidade is built as a frame
157 structure formed by steel beams having thin-walled hollow rectangular box section: for such structural
158 elements warping might play an important role and must be taken into consideration. Instead, the backup
159 structure supporting the primary mirror is a genuine truss structure formed by circular tubular struts, where no
160 warping can take place. Similar considerations hold true also for the quadrupode, formed by slender struts,
161 whose transversal to longitudinal size ratio makes warping negligible. Finally, each panel by which the Primary
162 Mirror is modelled by means of a four-node shell element capable of directly taking into account warping.

163 A summary of the number of elements and nodes that make up each part of the Finite Element Model is
164 presented in Table 1.

165

Macro-components	Number of Elements	Number of Nodes
Alidade	4380	4228
Cradle	13154	14695
Back Up Structure	60094	61872
Primary Mirror	1008	1104
Quadrupod	2882	3246
Secondary Mirror	24	16

166 *Table 1: Number of Elements and Nodes which each macro-component of Sardinia Radio Telescope's FE*
167 *model is composed*

168 The Alidade is symmetrical with respect to the z - y plane, see Figure 2, while no symmetries can be found in
169 the z - x plane.

170 The components with a structural role (Alidade, BUS and Quadrupod), have been modelled assuming that they
171 are made of isotropic steel with density $\mu_s = 7908.5 \text{ kg/m}^3$, Young's modulus $E_s = 199.95 \text{ GPa}$ and Poisson's
172 ratio $\nu_s = 0.29$. Its linear thermal expansion coefficient ψ_s is equal to $1.17 \times 10^{-5} \text{ }^\circ\text{C}^{-1}$. Steel is considered
173 linear elastic. At elevation angle of 90° SRT height is 68 metres. Overall, the FE model presents a total weight
174 of 31.730 MN. To describe the constraint conditions, it is useful to specify that the antenna moves on a plane
175 circular rail by means of eight bogies (four movement systems with two bogies each one) and rotates around
176 a central pivot.

177 The alidade structure has been assembled with millimeter accuracy while higher accuracy (sub-millimeter) has
178 been obtained for the main and secondary mirror.

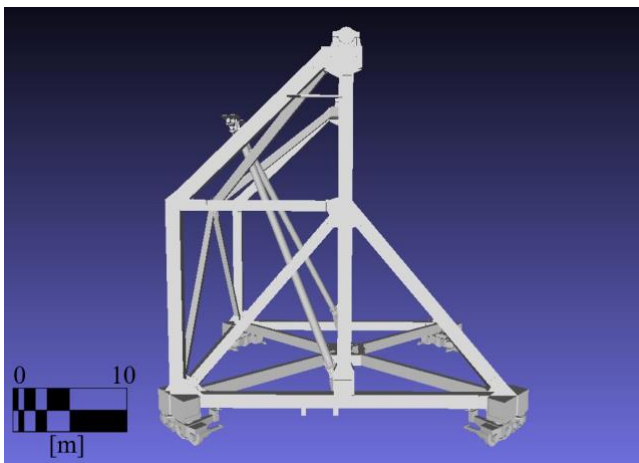
179 Therefore, in this work the effects produced by thermal loads have been described with the Pointing Vector
180 Rotation (PVR) parameter; it is expressed by Eq. (1):

$$181 \quad \text{PVR} = \sqrt{(\varphi_x)^2 + (\varphi_y)^2 + (\varphi_z)^2} \quad (1)$$

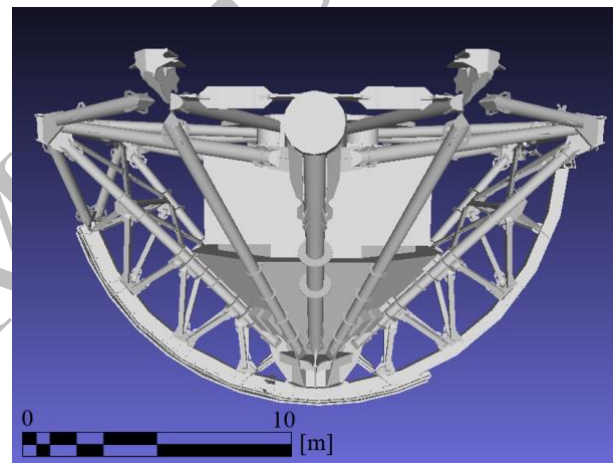
182 in which φ_x , φ_y and φ_z are the rotations of the pointing vector with respect to the ideal direction. They should
183 be zero in the ideal condition, while their values change as the pointing vector differs from the ideal position.

184 Given that the model is developed in a linear elasticity framework we can enforce the principle of overlapping
185 effects using an iterative approach. Indeed, by iteratively applying a thermal load of 10°C to each element of
186 the FE, it was possible to identify which one have the greatest impact on the pointing vector. The thermal
187 gradient produces a thermal expansion of the considered element, generating deformation of the structure.
188 Once the node where the pointing vector is located has been identified, its rotations can be evaluated
189 accordingly. Relating the value of the pointing error to the element subjected to the thermal gradient yields to
190 an element importance rank.

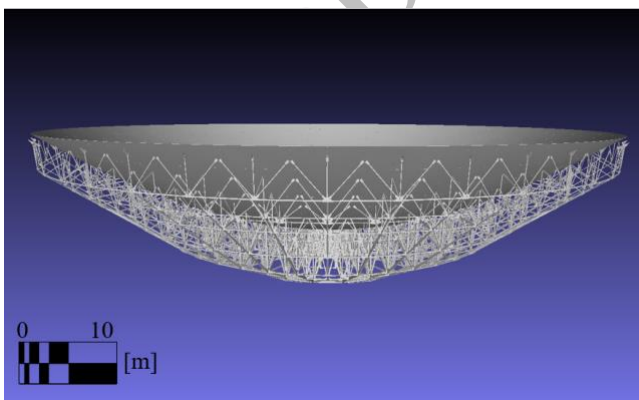
191 To simplify the problem, the Sardinia Radio Telescope has been divided into four macro-components (Alidade,
192 Cradle, Back Up Structure, Quadrupod) which are separately shown in the Figure 3:



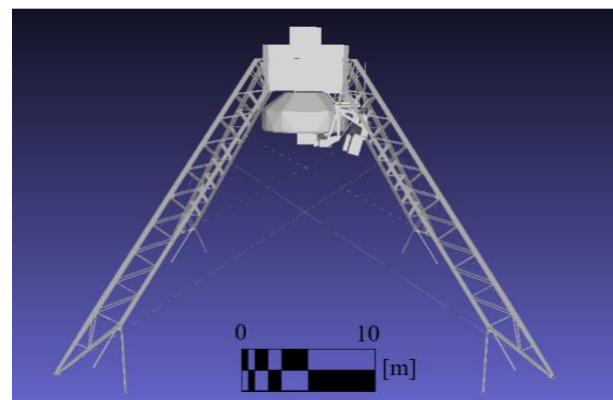
(a) Alidade



(b) Cradle



(c) Back Up Structure



(d) Quadrupod

193

Figure 3: SRT macro-components used for pointing error element ranking.

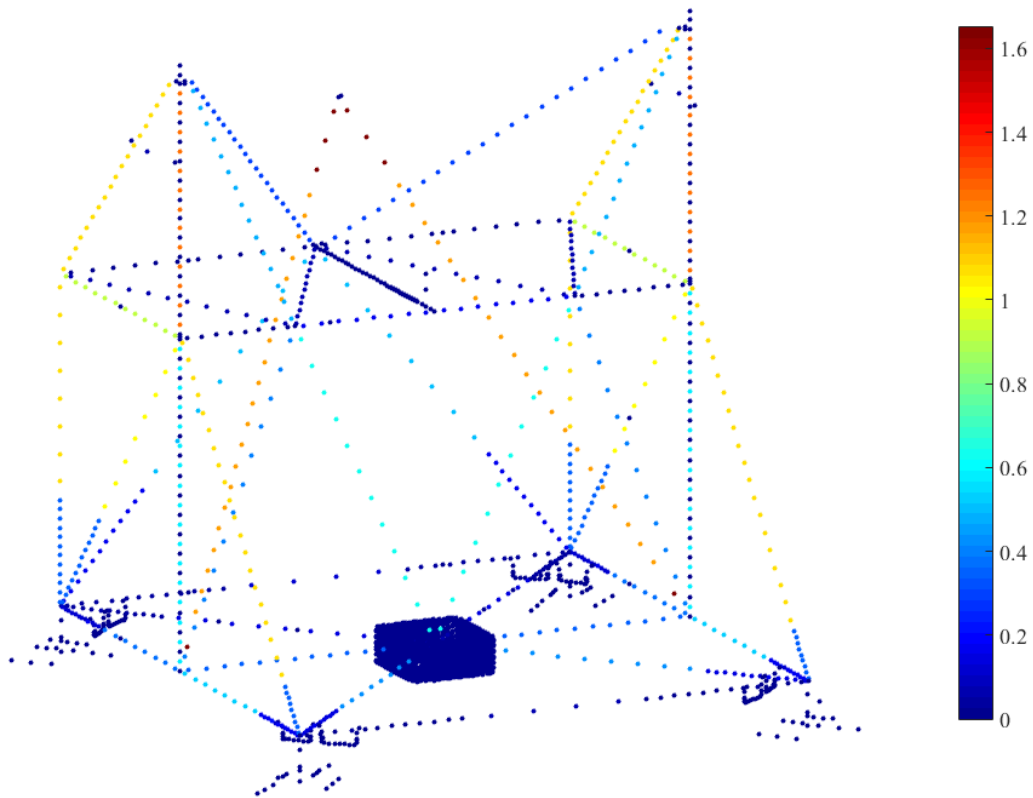
194

195 Figures 4-7 present the pointing error control parameter expressed in arcseconds, for each of the macro-
196 components analyzed with SRT at 90° elevation.

197 Looking at Figure 4 it is important to clarify that each point represents the element centre of gravity, while the
198 elevator has been represented by a set of point mass and for this reason some truss present more colour points
199 than others. Boundary conditions are represented by the solid basement model and by a set of kinematic
200 relationships between displacements and rotations on the rail base circle.

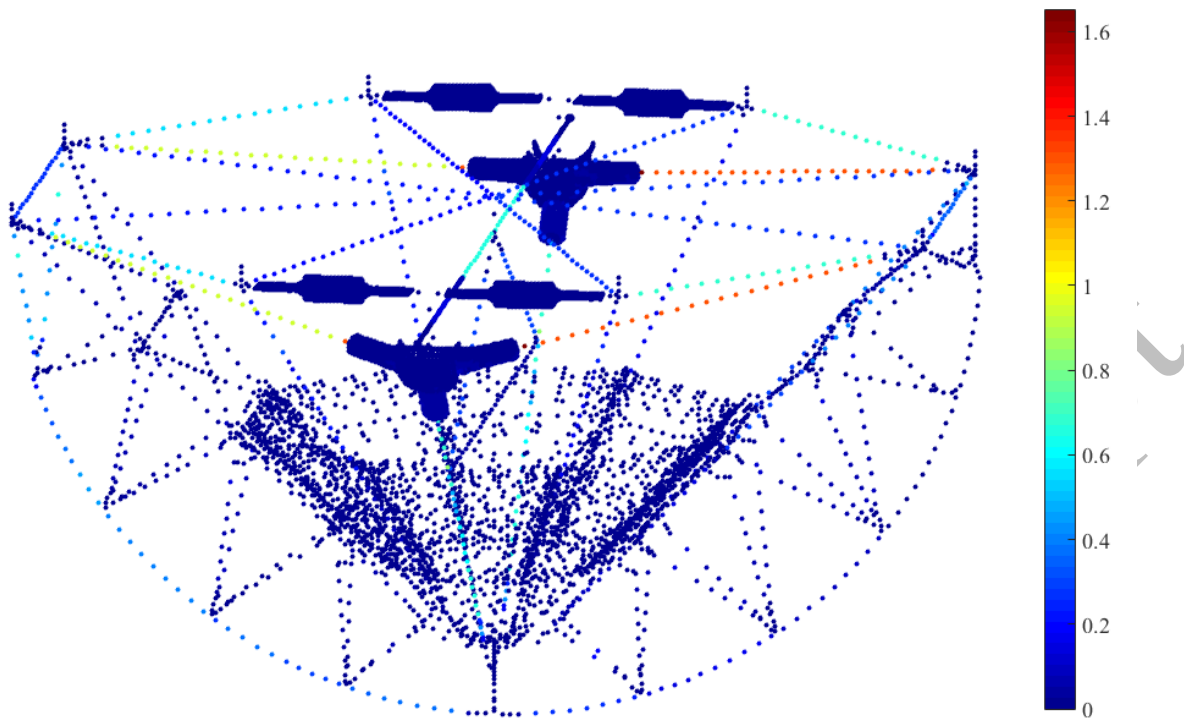
201

202



203

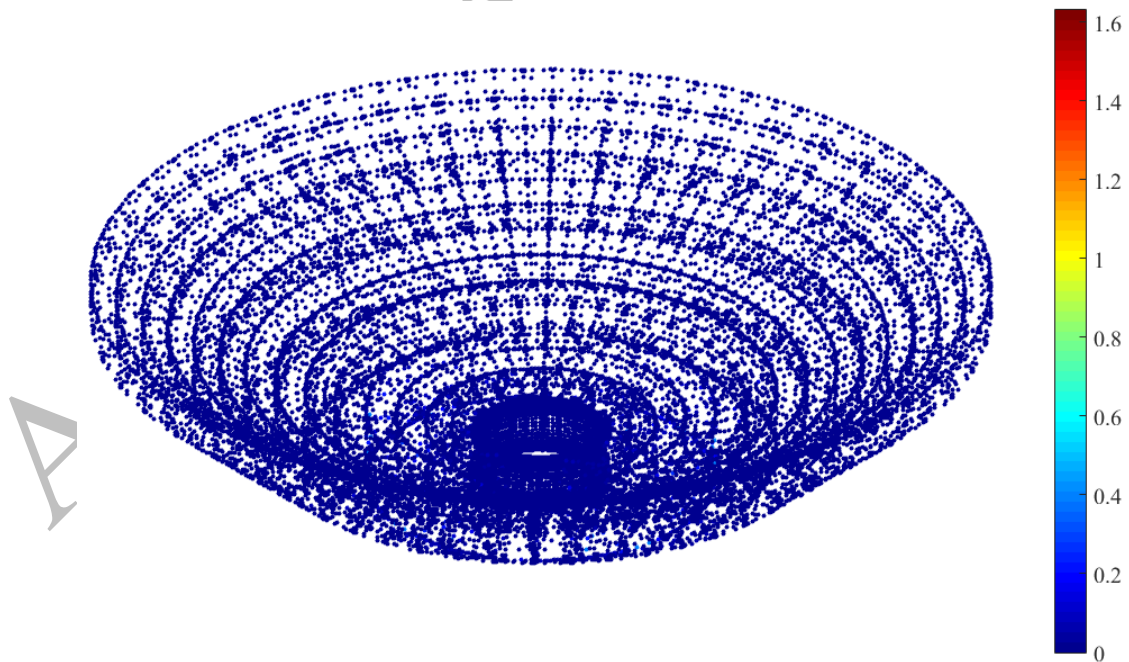
204 *Figure 4: Pointing Vector Rotation (in arcsec) for the Alidade's elements. Representation referred to 90 °*
205 *elevation.*



206

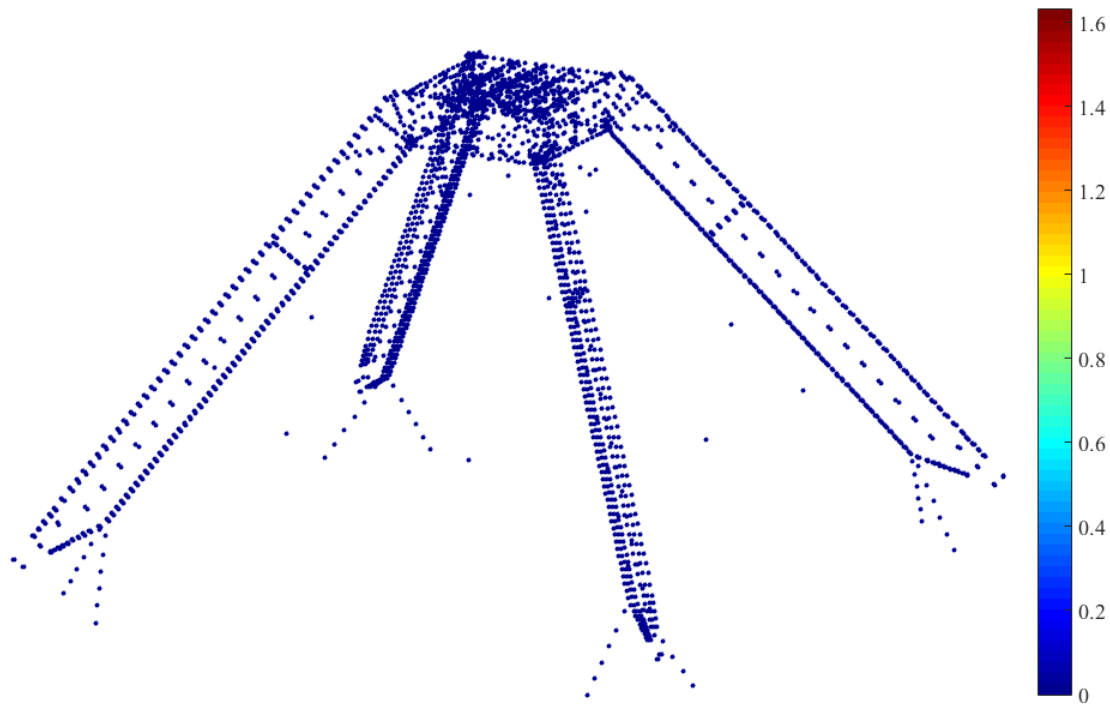
207 *Figure 5: Pointing Vector Rotation (in arcsec) for the Cradle's elements. Representation referred to 90 °*
 208 *elevation.*

209



210

211 *Figure 6: Pointing Vector Rotation (in arcsec) for BUS's elements. Representation referred to 90 ° elevation.*



212

213 *Figure 7: Pointing Vector Rotation (in arcsec) for the Quadrupod's elements. Representation referred to 90 °*
 214 *elevation*

215

216 The results presented by Figures 4-7 show that the alidade produces the greatest pointing errors in case of
 217 thermal load. Furthermore, the contribution offered by the Cradle should not be overlooked. Minor influence
 218 is instead produced by Back Up Structure and Quadrupod.

219 Therefore, these results suggest that the Alidade is the component of the radio telescope on which it is
 220 appropriate to focus more attention in this study, and provide an element ranking for pointing error produced
 221 by the thermal load. This aspect is of particular interest when it is necessary to identify the most suitable
 222 position to install thermal sensors.

223 Other sensitivity analyses, not reported here for the sake of synthesis, showed that different elevation angles
 224 (90 °, 60 ° and 30 °) present similar results.

225

226 3. Pointing Vector Rotation for uniform temperature distribution

227 In this section the rotation of the pointing vector has been studied in case of uniform temperature distributions
228 in the 49 trusses of the Alidade. Studying this condition allows us to analyse the behavior of the structure under
229 a uniform thermal load, neglecting the effects of shading and considering only geometrical and thermo-
230 mechanical characteristics.

231 Three load cases were analyzed with 90 ° antenna elevation and the uniform temperature gradient equal to
232 5°C, 10°C and 15°C. The values of the components that generate the total rotation of the pointing vector are
233 reported in Table 2. As already presented in the introduction the SRT minimum resolution at maximum
234 frequency is 1 arcsec. The small values of φ_y and φ_z can be explained considering the numerical errors of the
235 model.

T [°C]	φ_x [arcsec]	φ_y [arcsec]	φ_z [arcsec]
5	0.32542	0.00052	0.01248
10	0.65087	0.00104	0.02496
15	0.97629	0.00156	0.03743

236 *Table 2: Rotation components of the Point vector for different uniform temperature distributions (5 – 10 – 15*
237 *[°C]).*

238 The numerical values shown in the Table 2 indicate that the rotation around the x -axis is predominant over the
239 others in all three analyzed cases: two orders of magnitude with respect to φ_y and one order of magnitude with
240 respect to φ_z . This is due to the structural symmetry of the Alidade. Actually, symmetrical elements produce
241 rotations around the x -axis with the same direction, while the rotations around the y and z axes are both
242 discordant; thus, φ_y and φ_z tend to cancel out each other in the case of uniform thermal load in symmetric
243 trusses. The rotation around the elevation axis (x -axis) is instead linked to the difference between the number
244 of trusses that produce positive φ_x and the number of those that produce negative φ_x ; it is therefore
245 independent from the structural symmetry with respect to the z - y plane of the Alidade. In addition, it is
246 important to remember that no-symmetry is present with respect to the z - x plane.

247 In order to evaluate what has been described in a qualitative way, it is necessary to introduce a coefficient of
248 influence that takes into account the effects on the pointing vector produced by each element when subjected
249 to positive thermal load. This is necessary to obtain weighted temperatures for the trusses, preventing
250 temperatures applied to elements that produce important positive rotations from being cancelled out by
251 temperatures applied to trusses that instead produce opposite effects that produce smaller pointing errors.

252 We introduce the Influence Coefficients (IC) for the three rotation components for each of the 49 trusses. These
253 IC are obtained by dividing the rotation component ($\varphi_x, \varphi_y, \varphi_z$) of the pointing vector produced by each element
254 with respect to the maximum value found for the same rotation component. Having found the maximum value
255 of $\varphi_x, \varphi_y, \varphi_z$ among all trusses, it is possible to calculate the IC parameter of the j -th truss for the i -th rotation
256 component by dividing φ_{ij} by the absolute value of maximum φ_i ($|\varphi_{i-max}|$).

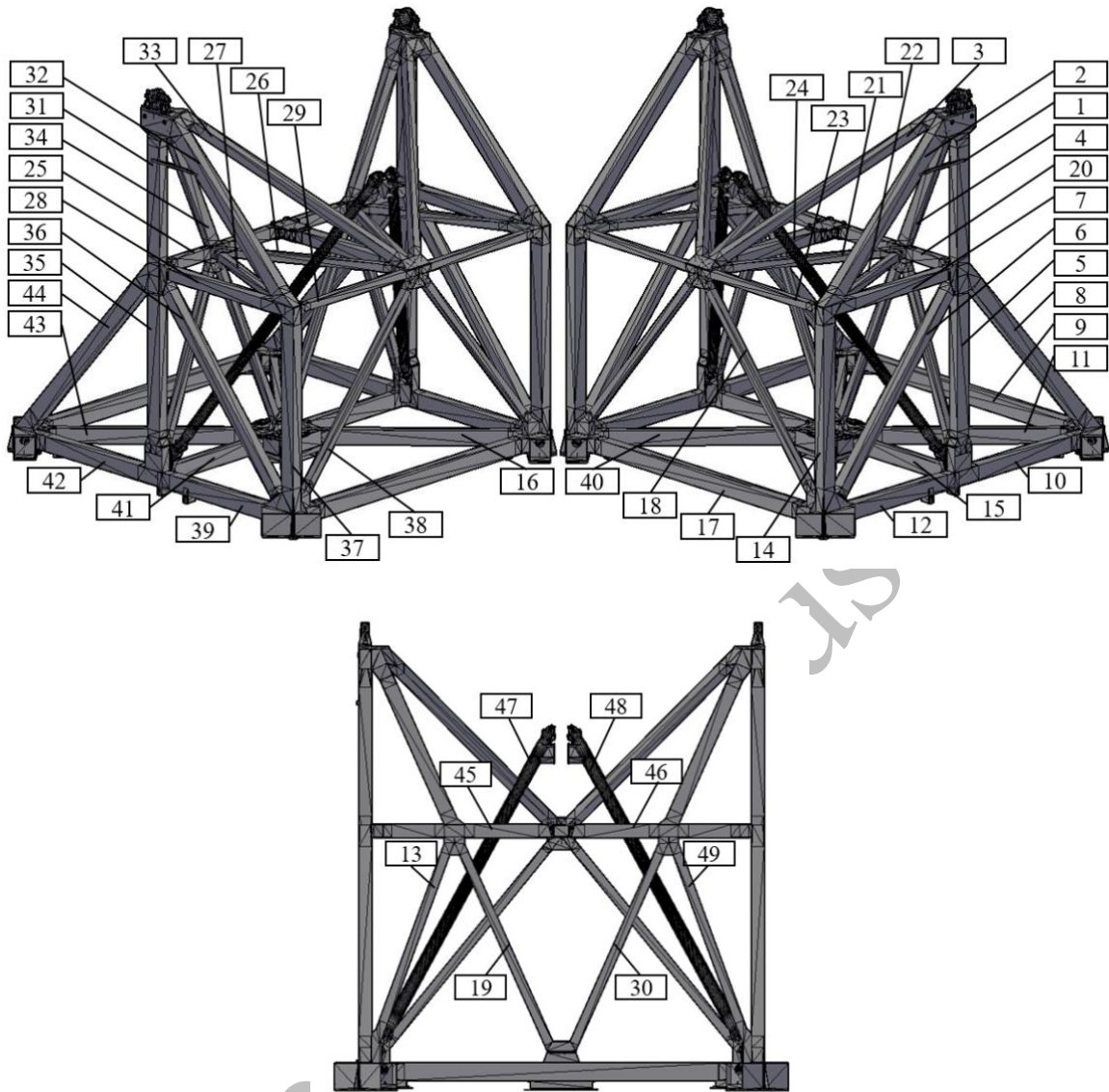
257 The Weighted Temperature is estimated by multiplying the temperature applied to each element by the
258 respective IC.

259 The algebraic sum of the weighted temperatures defines the total thermal gradient among the set of trusses that
260 produce positive rotations and those that produce negative rotations (2).

$$261 \quad \text{WTG}_i = \sum_{j=1}^{49} \text{IC}_{ij} T_j \quad (2)$$

262 Eq. (2) expresses the Weighted Thermal Gradient for the i -th rotation component ($i = x, y, z$), in which the
263 subscript j indicates the numerical labels of the trusses (see Figure 8).

264



265

266

267

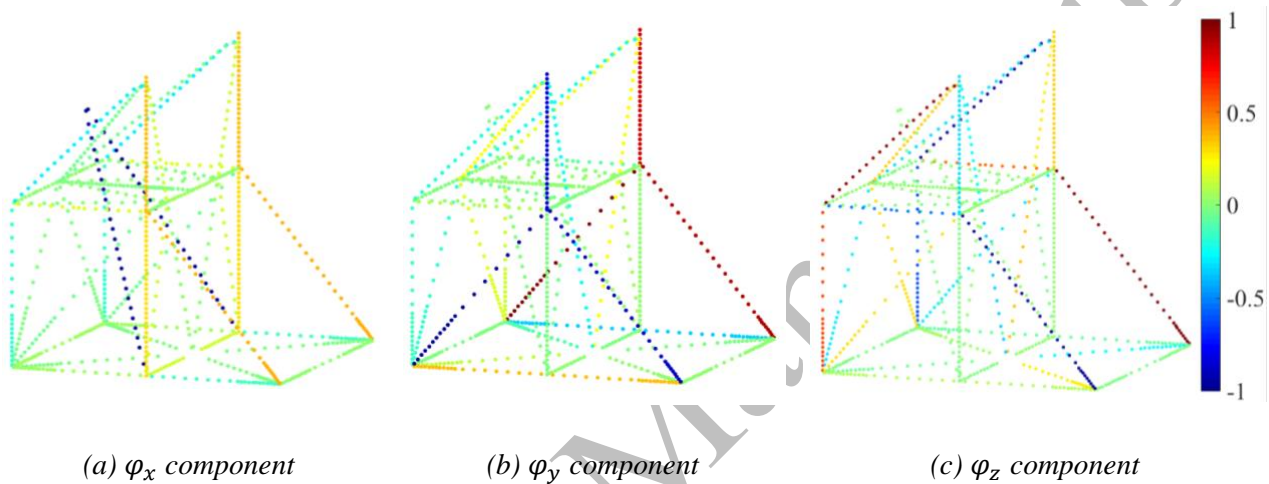
268

269 Figure 9 shows the values of the IC referred to each Alidade truss element, and for each rotation component
 270 (φ_x , φ_y and φ_z): the color of each point represents the truss IC value of which is part. Figures 10-12, which
 271 are referred respectively to x , y and z rotation components, shows the Weighted temperature for all uniform
 272 temperature distributions analyzed (5 – 10 – 15 [°C]): the color of each point represents the truss Weighted
 273 temperature value of which is part. Moreover Table 3 presents the values of the WTG for each rotation
 274 component, which are produced by the three uniform temperature distributions considered.

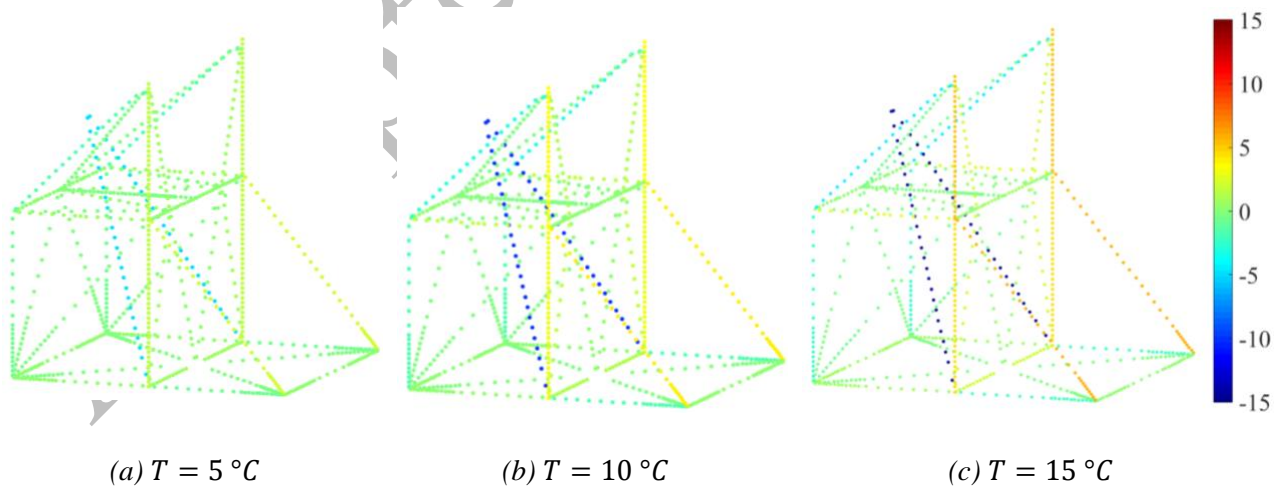
275 It can be noted that the WTG referred to the rotation around the x -axis is higher than the one that produce
276 rotations around the y and z axes, this can be explained with the effects of geometric symmetry described
277 above.

278 With reference to the rotation around the x -axis, there is an upward trend of the WTG with the increase in
279 temperature applied to the trusses, which justifies the increase in the total rotation of the pointing vector.

280

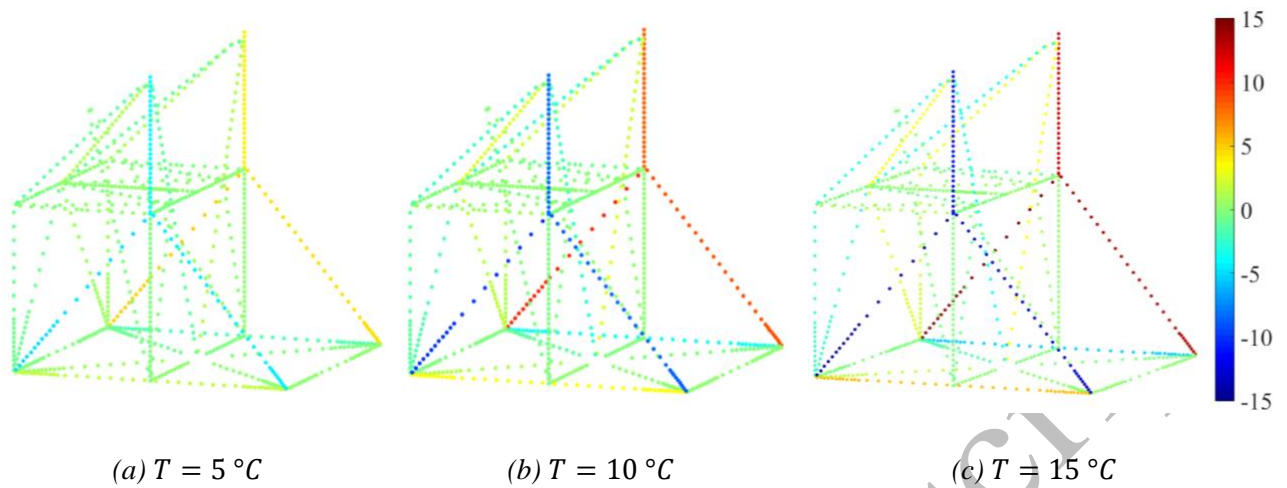


281 *Figure 9: Values of the Influence Coefficient (IC) on the pointing produced by alidade truss elements, for each*
282 *rotation component (φ_x , φ_y and φ_z).*



283

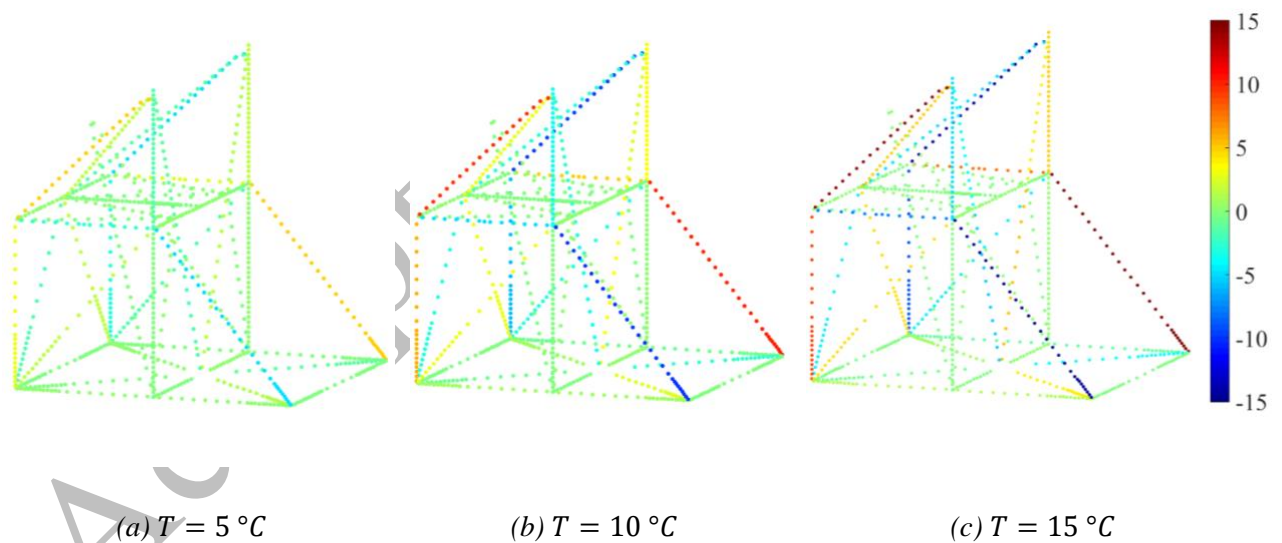
284 *Figure 10: Weighted temperature for different uniform temperature distributions (5 – 10 – 15 [°C]) – φ_x*
285 *component.*



287

288 *Figure 11: Weighted temperature for different uniform temperature distributions (5 – 10 – 15 [°C]) – φ_y*
 289 *component.*

290



291

292 *Figure 12: Weighted temperature for different uniform temperature distributions (5 – 10 – 15 [°C]) – φ_z*
 293 *component.*

Uniform Temperature distribution		T=5°C	T=10°C	T=15°C
WTG for the rotation components	x-component	0.10194	0.20387	0.30581
	y-component	0.00046	0.00092	0.00138
	z-component	0.00659	0.01319	0.01978

294 *Table 3: Weighted Thermal Gradient for all uniform temperature distributions analyzed (5 – 10 – 15 [°C]),*
 295 *referred to each rotation component.*

296

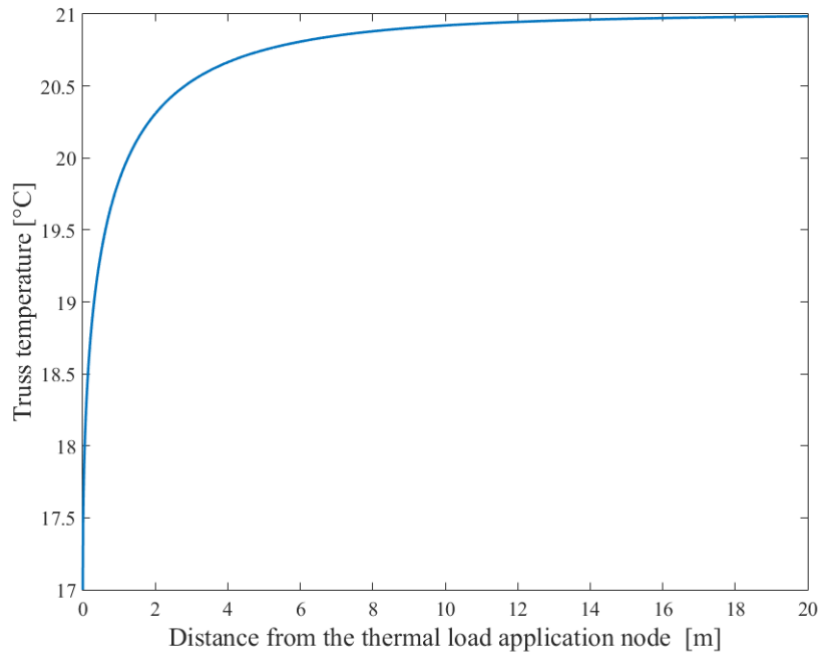
297 4. Heat balance model

298 The aim of this section is to obtain an analytical model capable of simulating realistic thermal scenarios due
 299 to environmental conditions and estimating the effects on the antenna pointing error.

300 Heat can be transferred by means of conduction, convection and radiation. The simultaneous heat propagation
 301 by convection and radiation is called thermal adduction. Temperature variation of SRT's structural elements
 302 are inevitably produced by these thermal phenomena.

303 In addition, given the characteristics of our case it is possible to ignore conduction effects in long elements
 304 such as alidade trusses. For example, Figure 13 shows the rapid decrease of temperature in a 20m steel truss
 305 subjected to a thermal load of -3°C at one end with environmental temperature of 21°C. The parameters that
 306 play a role in this case are the thermal conductivity of the steel and the coefficient that takes into account the
 307 heat transfer between the truss and the environment. The characteristic values suggested in the literature have
 308 been adopted: conductivity equal to 52 [W/(m K)] and heat transfer coefficient equal to 20 [W/(m²K)]. It can be
 309 seen that after almost one third of the span the truss temperature is almost constant, and it is similar to the
 310 environmental one. Thus, in the following we will ignore heat conduction among trusses that converge in the
 311 same node and will consider only convection and radiation.

312



313
314 *Figure 13: Temperature distribution in alidade steel truss under conductivity thermal load.*

315

316 When the radiative flux is incident on a surface, part of it is reflected. Therefore, the energy that leaves the
317 surface consist in the algebraic sum of reflected radiation and emitted radiation. Instead, the non-reflected
318 radiation energy penetrates the considered object and, crossing it, undergoes an attenuation. The part of it that
319 crosses the object is called transmitted radiation, and the difference is called absorbed radiation.

320 For a given surface, the relevant reflection coefficient ρ , transmission coefficient τ , and absorption coefficient
321 α , can be defined. However, most of solids are defined as opaque and they don't transmit thermal energy $\tau =$
322 0, but they only absorb it and reflect it, so that the remaining parameters are related by Equation (3)

323
$$\alpha + \rho = 1 \quad (3)$$

324 Considering short time intervals, it is possible to simplify the problem by assuming stationary conditions. Thus,
325 the evaluation of the energy exchanged can be described through an energy balance on a control volume. There
326 are examples of the use of this approach in the literature. In (Prado and Ferreira, 2005) the heat balance
327 equation is used to calculate the surface temperature of roofs in Brazil for an estimate of albedo; in (Vox et al.,
328 2016) the study of passive systems for the control of the thermal gain caused by sunlight is addressed; in

329 (Höppe, 1993) the energy balance is used to describe in detail the environmental thermal effects on the human
Please cite this document as: Attoli, A., Stochino, F., Buffa, F., Poppi, S., Serra, G., Sanna, G., & Cazzani, 19
A. (2022). Sardinia Radio Telescope structural behavior under solar thermal load. *Structures*, 39: 901-916.
DOI: [10.1016/j.istruc.2022.03.065](https://doi.org/10.1016/j.istruc.2022.03.065)

330 body; (Bhumralkar, 1975) analyzes the energy exchange between the atmosphere and the soil under different
 331 conditions of radiation influence by integrating the Rand two-level general circulation model.

332 If the considered surface is opaque, the heat balance equation is (Höppe, 1993):

$$333 \quad \dot{Q} = A(ER + \rho G - G) \quad (4)$$

334 where \dot{Q} is the net thermal power transferred from the surface A to the environment by radiation only; ER is
 335 the thermal radiation emitted by the surface A which can be estimated through the Stefan-Boltzmann law for
 336 real bodies (7):

$$337 \quad ER = \varepsilon \sigma T_p^4 \quad (5)$$

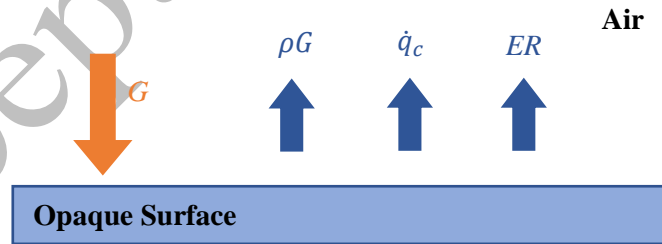
338 where ε is the emissivity, σ is the Stefan-Boltzmann constant (6)

$$339 \quad \sigma = 5,67 \cdot 10^{-8} \left[\frac{W}{m^2 K^4} \right] \quad (6)$$

340 T_p is the surface A temperature, G is the solar radiation that strikes the same surface and ρG is the rate of
 341 reflected solar radiation. If we take into account the convection effects:

$$342 \quad \dot{Q}_c = A \dot{q}_c = A h_c (T_p - T_a) \quad (7)$$

343 where \dot{q}_c denotes the convection flux between the surface A and the environment, h_c is the convection
 344 coefficient between the same surface and the air, T_p is still the surface temperature and T_a is the environmental
 345 temperature.



346 *Figure 14: considered terms in the energy balance.*

347
 348 Expressing the terms indicated in Figure 14 and in Eq. (4) and Eq. (7) for a unit surface (i.e. $A=1$), yield Eq.
 349 (8) and (9):

$$350 \quad G = \rho G + \dot{q}_c + ER \quad (8)$$

$$G = \rho G + h_c (T_p - T_a) + \varepsilon \sigma T_p^4 \quad (9)$$

The reflection coefficient $\rho = (1 - \alpha)$ and the emissivity ε are expressed as a function of the surface conditions of the real body. For a white paint surface treatment as in the examined case, we can assume the following values for emissivity, absorption coefficient and reflection coefficient respectively: $\varepsilon = 0.88$, $\alpha = 0.14$, $\rho = 0.86$ (Kosky et al., 2013).

The convection coefficient is expressed in relation to the fluid where the thermal energy exchange takes place and to the stationary level of the fluid. If the fluid is not forced air, h_c assumes values between 2.5 and 25 $W / (m^2 K)$ (Kosky et al., 2013); in this case it is set equal to 20 $W / (m^2 K)$.

Once the solar radiation G and the environmental temperature T_a have been identified, an algebraic equation of 4th degree in the unknown T_p is obtained, see Eq. (9), which can be solved by an iterative method.

5. Solar radiation analysis

The commercial Autodesk Revit software (Khemlani, 2004) was used to estimate the solar radiation that reaches each truss of SRT. The use of radiation simulation software allows to consider shadows and reflections generated by the radio telescope components and to study the effects of solar radiation incident to a surface characterized by a given percentage of obscuration.

A database of climatic information, included in the software, allows to obtain a hourly profile of environmental temperatures, i.e. an essential piece of information in the proposed analytical model.

The incident solar radiation (I_i) is evaluated through Eq. (10)

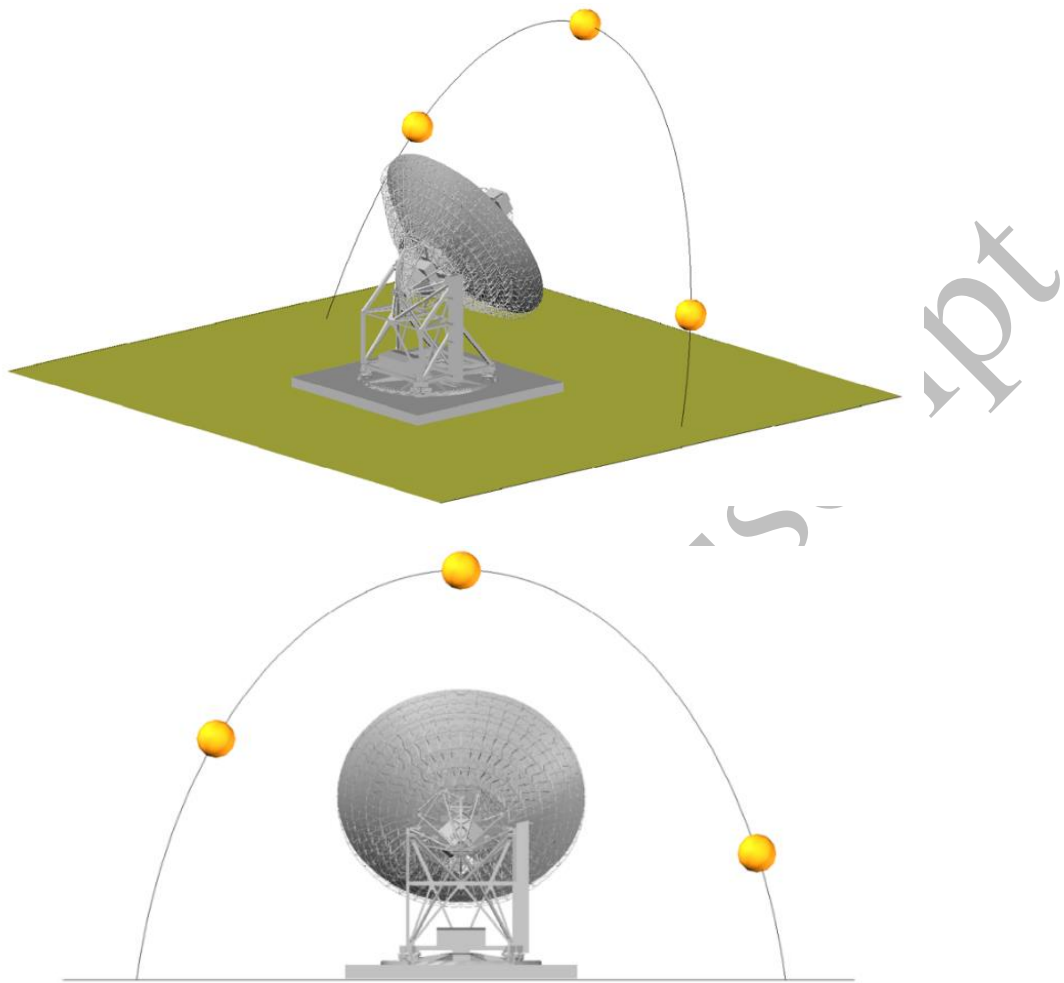
$$I_i = (I_b \cdot \cos \vartheta \cdot F_{sh}) + (I_d \cdot F_{sk}) + I_g \quad (10)$$

where I_b is the direct beam radiation which is measured perpendicular to the sun, ϑ is the angle where beam radiation affect the surface, F_{sh} represent the fraction of the surface currently in shadow from other surrounding geometry, I_d is the diffuse sky radiation, F_{sk} is the fraction of the diffuse sky visible in this instant from the

374 surface and I_g is the radiation reflected from the ground. Furthermore, the average value of radiations that
375 affects the four faces of the three-dimensional truss has been considered.

376 At the end of the analysis, the total radiation relative to each daytime hour of the day is obtained; this piece of
377 information is then used for the calculation of each element temperature using the model presented in Section
378 4. Figure 15 shows how the different position of the sun produces variable shading during the day. Obviously,
379 an important role is played by the orientation and elevation angle of the antenna. The extent of solar radiation
380 depends on all these aspects; it is clear how all this affects each antenna truss which will have a different
381 temperature compared to the others in every situation. It is interesting to perform simulations for different
382 configurations in terms of elevation, orientation and day of the year. In the following Section 6 the model
383 calibration is performed considering the following dates: September 11th 2020, November 19th 2020,
384 December 31th 2020. While in Section 7 each season (February 5th Winter, May 5th Spring, August 5th
385 Summer, and November 5th Fall) is considered for the case studies.

Accepted Manuscript



387

388

Figure 15: Different sun positions throughout the day, compared to Sardinia Radio Telescope

389

6. Calibration of heat balance equation parameters

390

391

In the preliminary phase, the values of the reflection coefficient ρ , absorption coefficient α and emissivity ε mentioned in the Section 4 were used. However, these are ideal values that may differ from the real ones.

393

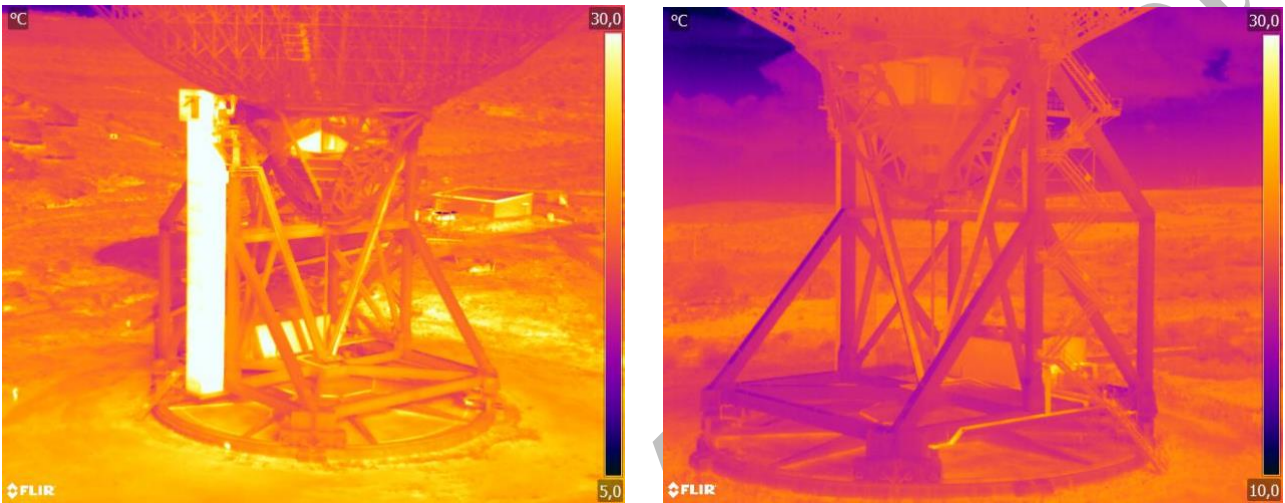
Indeed, the state of the coating with which the structure was treated shows imperfections due to normal atmospheric agents and oxidation typical of metal systems. These defects alter the ideal values of the

395

parameters involved, influencing the temperature calculation.

396 In order to obtain realistic temperature values, a calibration of the reflection coefficient ρ and emissivity ε was
397 carried out. This was made possible by using the data collected with a thermal imaging camera housed in a
398 drone (see Figure 16).

399 The Flir Zenmuse XT thermal imaging camera was used for all investigations; it can operate in -25°C to
400 $+135^{\circ}\text{C}$ scene range. When environmental conditions are ideal, this device provides an accuracy of $\pm 5^{\circ}\text{C}$.



401
402 *Figure 16: Thermal images captured by the drone.*

403
404 Three surveys were carried out, in the daytime hours of September, 11th 2020, November, 19th 2020 and
405 December, 31th 2020.

406 The images were taken on the four sides of the radio telescope in order to frame and characterize an adequate
407 number of trusses which are useful for validating the model.

408 A local temperature measurement of the lower trusses (trusses that are located at eye level) was also performed,
409 using an infrared thermometer in order to validate the temperatures measured with the thermal camera.

410 To estimate the real temperature of each truss, the average of the values of the visible 4 sides was evaluated.

411 In addition, the temperature on each side of the truss was estimated as the average of the measurements in
412 three points: in the center and at both ends (see Figure 17).

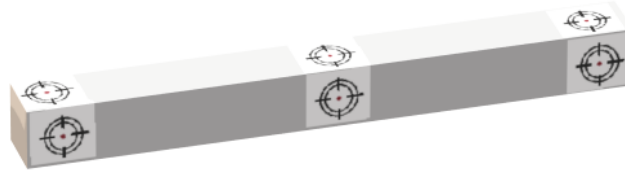


Figure 17: Point of elements where temperatures were measured.

413

414

415

416 The theoretical temperatures were calculated using the solar radiation values provided by the solar radiation
 417 model presented in Section 5 and the heat balance model presented in Section 4.

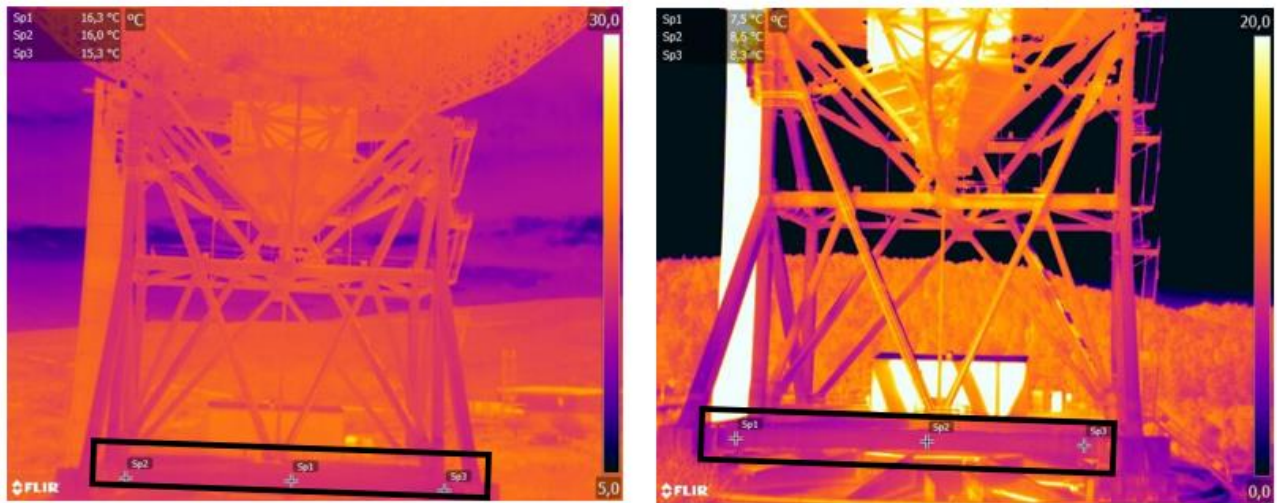
418 The values of the emissivity ε and reflection coefficient ρ were obtained with a least squares approach
 419 comparing the temperatures measured on site, which are adopted as benchmark, and the temperatures
 420 simulated with the analytical model. In this way, the following values for emissivity, reflection coefficient and
 421 absorption coefficient respectively were defined: $\varepsilon = 0.65$, $\rho = 0.60$, $\alpha = 0.40$.

422 Table 4 shows the comparison between measured and simulated temperatures for the trusses indicated in the
 423 thermal images (Figures 18-19) which are related to surveys carried out in two different campaigns: September,
 424 11th 2020 on the left side and November, 19th 2020 on the right side.

425

Truss N°	Date	Local Time	Detected Truss		Simulated Truss		Date	Local Time	Detected Truss		Simulated Truss	
			Temperature [°C]	Temperature [°C]	Temperature [°C]	Temperature [°C]			Temperature [°C]	Temperature [°C]		
8	11-set	10:00	16.5	17.2	19-nov	09:00	7.5	8.0				
9	11-set	10:00	15.5	15.8	19-nov	09:00	7.0	7.5				
44	11-set	10:00	17.5	17.9	19-nov	09:00	8.0	8.1				

426 Table 4: Simulation data for the two cases mentioned in the example. The Detected Truss Temperature is the
 427 average value of the temperature range measured at the points specified in Figure 17.

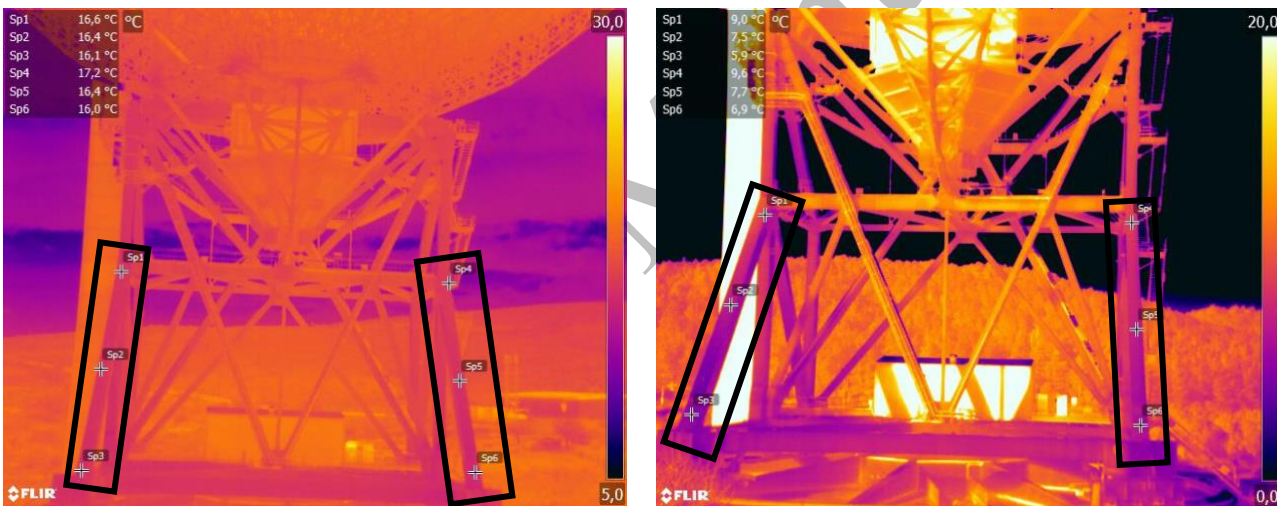


428

429

Figure 18: Location of Sardinia Radio Telescope truss n°9 mentioned in the example.

430



431

432

Figure 19: Location of Sardinia Radio Telescope trusses n°8 (on the left side) and n°44 (on the right side),

433

mentioned in the example.

434

435

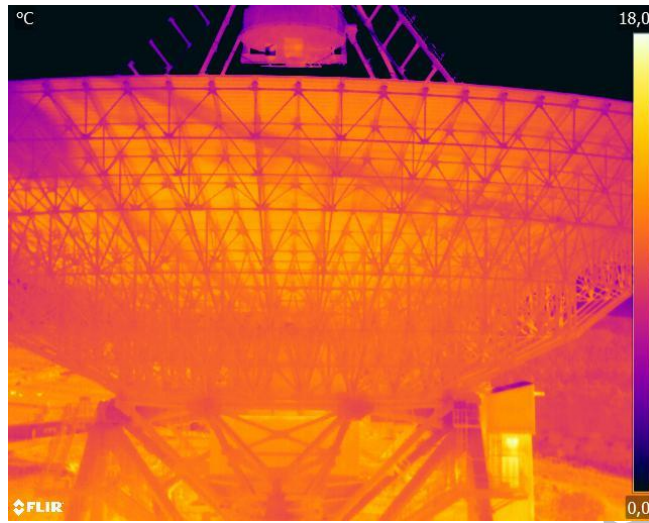
Table 5 shows the difference between simulated temperatures and temperatures measured in three different

436

surveys for some of the 49 trusses of the alidade.

11/09/2020 $T_a=20^\circ\text{C}$			19/11/2020 $T_a=15^\circ\text{C}$		31/12/2020 $T_a=7^\circ\text{C}$	
Rod	Detected	Simulated	Detected	Simulated	Detected	Simulated
N°	T [$^\circ\text{C}$]	T [$^\circ\text{C}$]	T [$^\circ\text{C}$]	T [$^\circ\text{C}$]	T [$^\circ\text{C}$]	T [$^\circ\text{C}$]
1	16.4	17.4	8.2	8.0	0.8	0.0
8	16.4	17.2	7.4	8.0	1.0	0.0
9	15.8	15.8	7.0	7.5	0.4	-0.3
10	15.7	15.8	7.7	7.5	-0.2	-0.3
12	15.7	16.0	7.8	7.5	-0.1	-0.3
28	16.4	16.0	7.0	7.4	0.6	-0.4
31	16.7	17.4	8.2	8.0	0.5	0.0
32	17.1	16.3	8.0	7.7	-0.3	-0.2
35	17.1	17.4	8.2	8.0	0.8	0.0
36	17.3	16.8	8.0	7.9	0.8	0.0
37	17.0	17.4	7.8	8.0	0.2	0.0
44	17.1	17.9	8.1	8.0	0.4	0.0
45	16.4	16.0	7.9	7.5	0.1	-0.3
46	16.4	16.0	7.9	7.5	0.1	-0.3

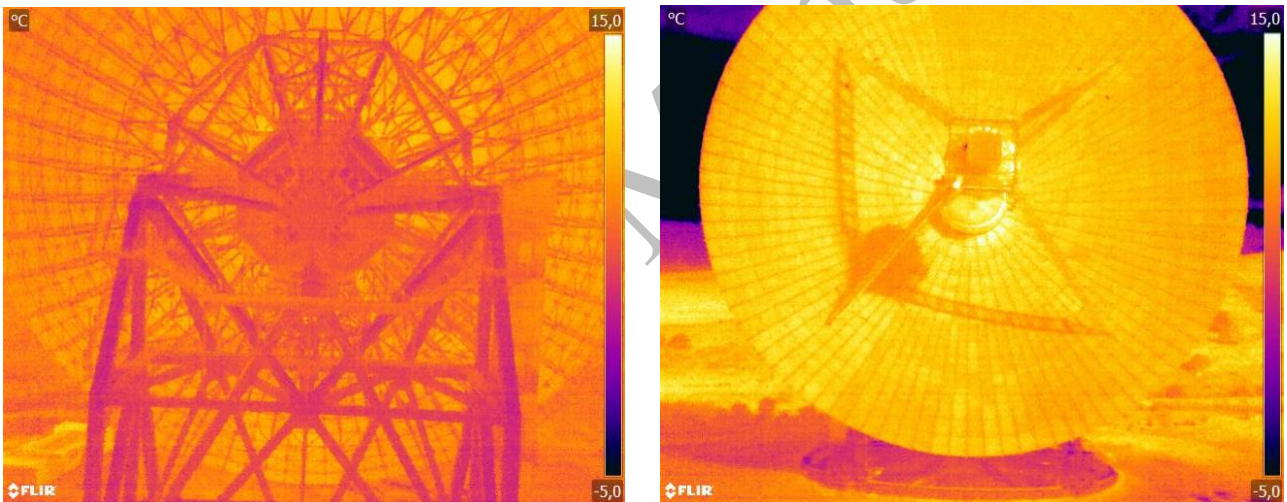
437 Table 5 : Comparison between simulated and detected temperature in three different surveys for some trusses
438 of the Alidade.



440

441

Figure 20: Thermal images captured by the drone on November 2020



442

443

Figure 21: Thermal images captured by the drone on December 2020

444

445 Furthermore, in Figures 20-21 it is possible to see that the active surface panels can be significantly hotter than
 446 the alidade, BUS and Cradle trusses; the effect is due to the shading generated by the parabolic mirror.

447 Once the parameters were calibrated, each set of simulated temperatures corresponding to a given scenario can
 448 be applied to the finite element model for the calculation of the focus pointing error.

449

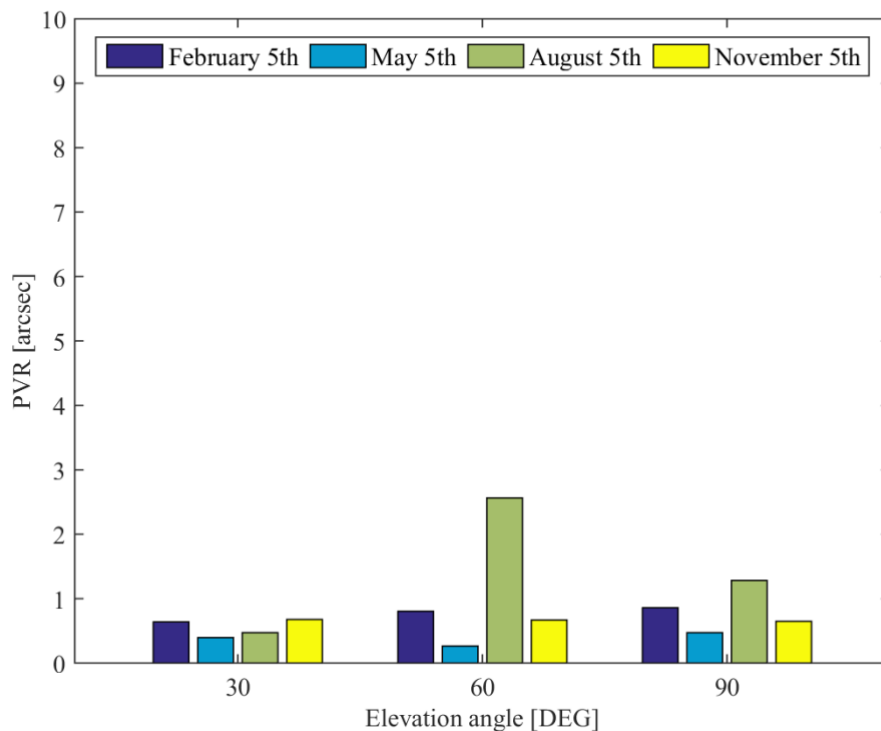
450 7. Numerical results.

451

452 Given the results of the sensitivity analysis described in Section 2, our attention was focused on the effects of
453 irradiation on the alidade trusses and on how this affects the pointing vector of the radio telescope.

454 In particular, in four representative days of each season of the year (February 5th, May 5th, August 5th and
455 November 5th) that falls in the middle of the respective season (Winter, Spring, Summer, Fall), 9 simulations
456 were performed: three elevation angles of the parabola, 90 °, 60 ° and 30 °, three orientation of the parabola in
457 the North, East and South direction were considered.

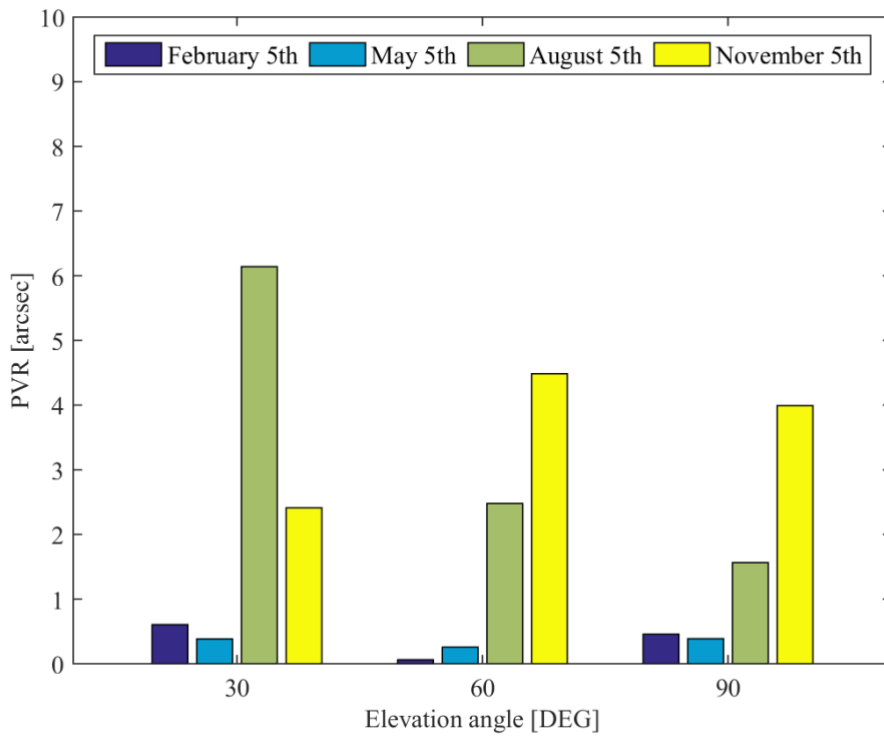
458 The combinations have been chosen to represent most of the possible scenarios in which the Sardinia Radio
459 Telescope operates, in order to represent its behavior in the four seasons. The simulations were developed
460 considering a reference local time (12:00) for all the analyzed cases. The values of Pointing Vector Rotations
461 (PVR) obtained for all the considered load scenarios are shown in Figures 22-24



462

463 *Figure 22: Point Vector Rotation (PVR) for the 4 analyzed days. (Configuration with NORTH Orientation).*

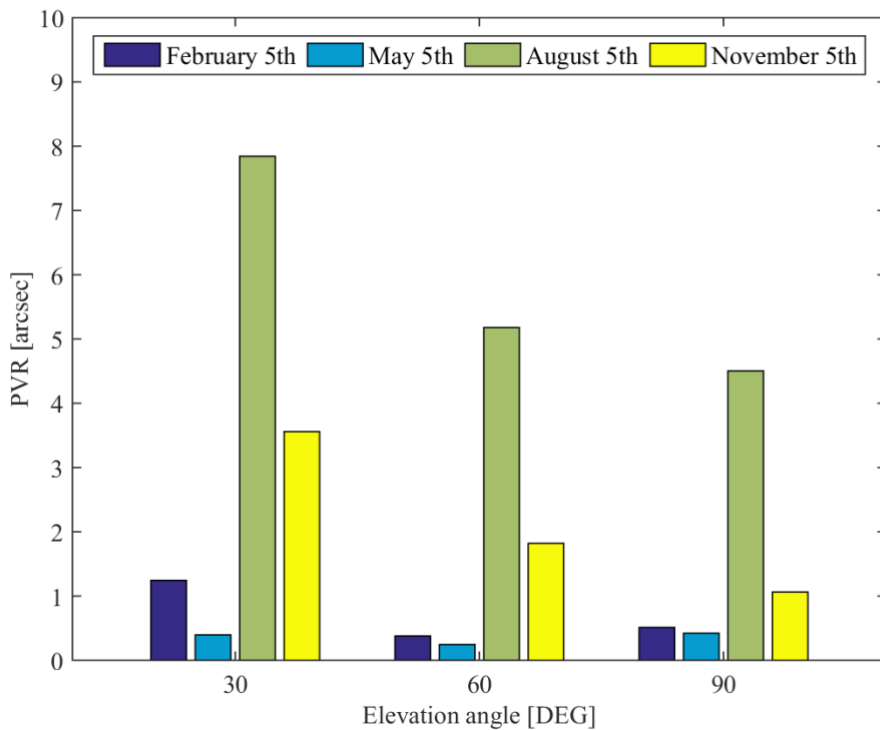
464



465

466

Figure 23: Point Vector Rotation (PVR) for the 4 analyzed days. (Configuration with EAST Orientation).



467

468

Figure 24: Point Vector Rotation (PVR) for the 4 analyzed days. (Configuration with SOUTH Orientation).

469

470 The diagrams show that thermal loads have an important influence on the SRT's structural behaviour, as it
471 affects its accuracy. It is also evident that the increase of environmental temperature during the year does not
472 inevitably produce an increase of the pointing error.

473 Table 6 presents the environmental and average truss temperatures for the South orientation.

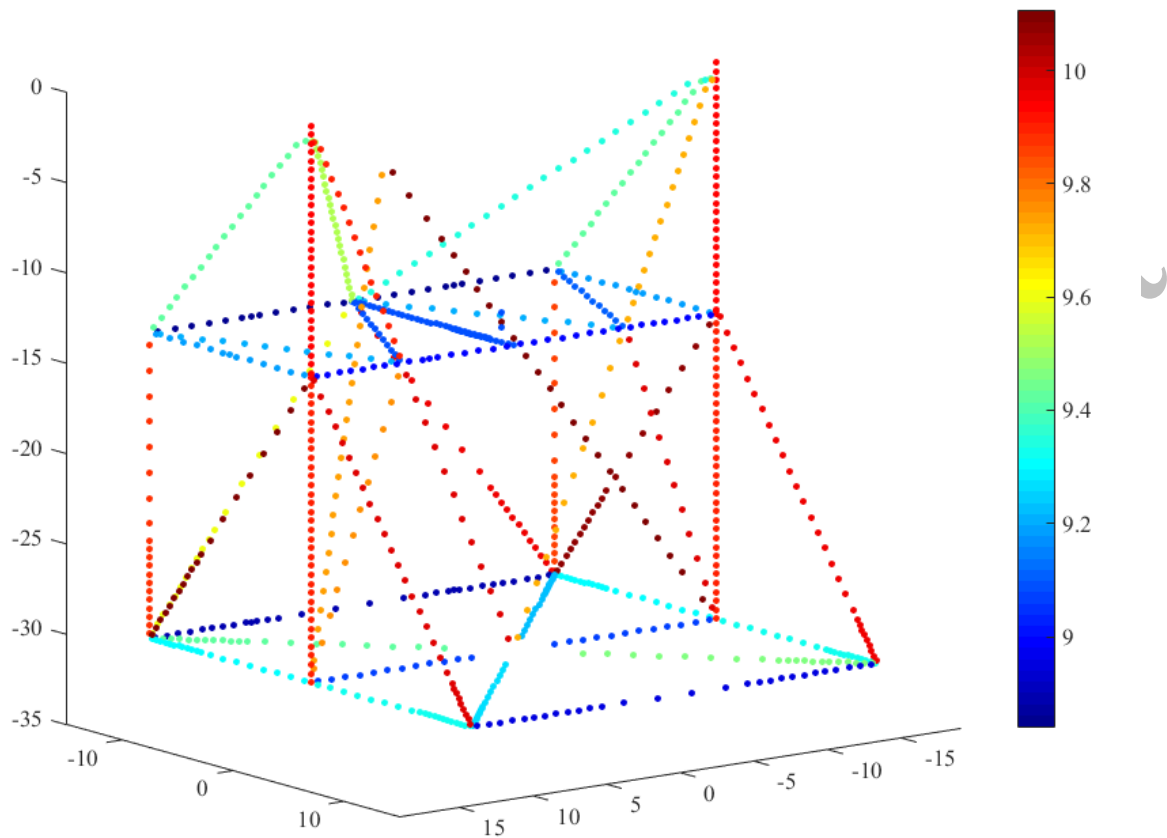
474

Accepted Manuscript

SOUTH ORIENTATION				
		30 ° Elevation	60 ° Elevation	90 ° Elevation
	Environmental	Average truss	Average truss	Average truss
Day	tempertaure	temperatures of the	temperatures of the	temperatures of the
		Alidade	Alidade	Alidade
	[°C]	[°C]	[°C]	[°C]
February 5th	14	9.48	9.45	9.43
May 5th	18	11.59	11.58	11.57
August 5th	28	22.37	22.44	22.39
November 5th	13	6.46	6.37	6.38

476 *Table 6: Values of Environmental temperature and Average truss temperatures of the Alidade. (Configuration*
 477 *with SOUTH Orientation).*

478



480

481 *Figure 25: Distribution of temperatures in the Alidade trusses referring to the case of Elevation 60 ° with*

482

EST orientation for February 5th. [°C]

483

Average Temperature	9.46956
---------------------	---------

Standard deviation of temperatures	0.39612
---------------------------------------	---------

484

485 *Table 7: Statistical data for temperature distribution applied to the Alidade's trusses.*

485

Pointing Vector Rotation Produced			
φ_x	φ_y	φ_z	PVR
[arcsec]	[arcsec]	[arcsec]	[arcsec]
-0.02692	-0.00026	-0.05578	0.06194

487

Table 8: Dataset of the Pointing Vector Rotation produced.

488

489 Figure 25 shows an example the distribution of temperatures in the Alidade trusses referring to the case of
 490 Elevation 60° with EST orientation for February 5th; the statistical parameters of the distribution are indicated
 491 in Table 7. Table 8 shows the values of the rotations produced by the thermal scenario applied to the FEM
 492 model; it can be seen that the rotation around the z rotation axis is of the same order of magnitude as the
 493 rotation around the x -axis. The lack of symmetry in the distribution of temperatures with respect to the y - z
 494 plane prevents φ_z rotations from cancelling each other out.

495

	x-component	y-component	z-component
	[°C]	[°C]	[°C]
Absolute value of (WTG) for the rotation components	0.04416	0.00124	0.03897

496 *Table 9: Order of magnitude of the Weighted Thermal Gradient for the rotation components of pointing vector.*

497

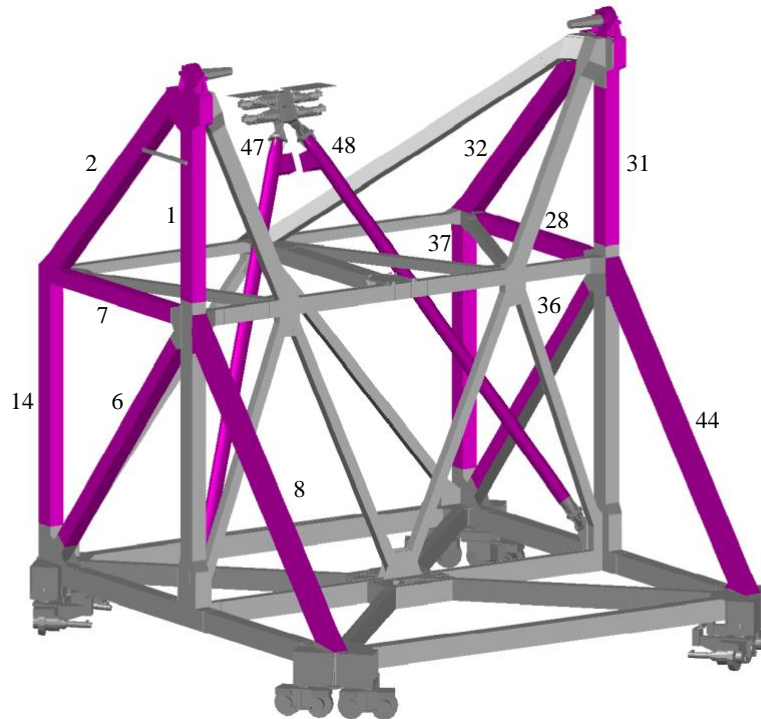
498 Table 9, related to the above described example, shows how the Weighted Thermal Gradient (WTG) of x -
 499 rotation is of the same order of magnitude to the one obtained for z rotation.

500 Looking at the obtained results, no trend related to the variation of seasonal environmental temperatures can
 501 be defined. Indeed, the dominant aspect is the different irradiation caused by the geometric configuration of
 502 the entire antenna.

503 8. Discussions and Conclusions.

504

505 In this paper, the effects on the pointing error of SRT produced by solar radiation acting on its structural system
506 have been studied. Through a sensitivity analysis it was possible to establish that the Alidade is the component
507 of the radio telescope that produces greater pointing errors when subjected to a thermal load. In addition, the
508 chromatic variation in Figure 4 makes it possible to recognize the level of importance of each Alidade truss.
509 In fact, the colour is linked to the value of the Pointing Vector Rotation (PVR) introduced in Eq. (1). Figure
510 26 highlights the most important trusses (n. 1, 2, 6, 7, 8, 14, 28, 31, 32, 36, 37, 44, 47, 48, see Figure 8), to
511 evaluate the thermal load effects on pointing error.



512



513 *Figure 26: Alidade's trusses that produces greater pointing errors when subjected to a thermal load.*

514

515 Then, an analytical model was used to estimate the temperature of the Alidade trusses, by means of solar
516 radiation determined with a numerical model that takes into account also the effects of convection.
517 Furthermore, the calibration of the analytical model parameters was performed by comparing the experimental

518 data deriving from thermographic investigations performed on the entire antenna. Using Finite Element
519 Analysis, the pointing error generated by each simulated thermal scenario was determined. Finally, the results
520 obtained made it possible to better understand the structural behavior of the Sardinia Radio Telescope under
521 simplified, but realistic thermal conditions.

522 Looking at the results for the South Orientation in Figure 24, it can be noted that the value of the Pointing
523 Vector Rotation in November is higher than the corresponding value in May for each elevation angle, despite
524 the average temperature of the trusses in spring is higher than that in autumn. The trend is not confirmed by
525 the data referring to August, in which case both maximum temperature value and maximum PVR are found
526 for this configuration (see Table 6). It is important to clarify that the average element temperatures obtained
527 by the solar irradiation model (Revit software and analytical model) are an approximation that requires the use
528 of the ANSYS FE model to evaluate the effects on the pointing vector error.

529 The phenomenon is therefore significantly influenced by the variable distribution of temperatures in the
530 Alidade elements. The shading given by the position of the sun with respect to the antenna and the elevation
531 of the parabola can result in a different irradiation of the trusses bringing them to uneven temperatures. In this
532 case, since trusses in a symmetrical position with respect to the z - y -plane are subjected to different thermal
533 load, the compensation of rotations around the y and z rotation axes due to the geometric symmetry of the
534 Alidade is lost (as discussed in Section 3). For these reasons, unlike the case of uniform temperature
535 distribution, φ_y and φ_z assume the same importance as φ_x , presenting the same order of magnitude.

536 When temperature distribution is not uniform, it is not possible to clearly delineate a trend for the total Pointing
537 Vector Rotations because it is conditioned by the combined effect of:

538 - the value of WTG_x which depends on the temperature difference among trusses that generate opposite
539 rotations around the x -axis;

540 - the values of WTG_y and WTG_z which depend on the temperature difference among the Alidade trusses
541 located in a symmetrical position with respect to the z - y -plane; they increase φ_y and φ_z rotations respectively.

542 In conclusion, the pointing error is more influenced by the shading than by the seasonal variation of the solar
543 radiation.

544 The need to continuously monitor the temperature of the trusses in order to forecast the pointing vector
545 variation arises from this analysis. Through a metrological system it is possible to acquire temperatures from
546 thermocouples distributed in optimal positions over the entire Alidade structure. In this way, the obtained data
547 can be processed in the finite element model for estimation, at any time, of the pointing error generated by
548 thermal conditions. This would allow to forecast the antenna pointing correction for a given set of loads.
549 It is interesting to point out that the whole metrological system of SRT will be based on a neural network that
550 will require training data. For this reason, the proposed methodology can produce useful training scenario for
551 the SRT neural network or for others similar systems extending the impact of this approach.
552

Accepted Manuscript

Symbol	Description
μ	Density
E	Young's modulus
ν	Poisson's ratio
ψ	Expansion coefficient
PVR	Point Vector Rotation
φ_x	Rotations of the pointing vector around the x -axis.
φ_y	Rotations of the pointing vector around the y -axis.
φ_z	Rotations of the pointing vector around the z -axis.
IC	Influence Coefficient
WTG	Weighted Thermal Gradient
ρ	Reflection coefficient
τ	Transmission coefficient
α	Absorption coefficient
ε	Emissivity
\dot{Q}	Thermal power transferred by radiation
A	Reference surface
ER	Thermal radiation emitted by a surface
G	Solar radiation
σ	Stefan-Boltzmann constant
T_p	Surface temperature
T_a	Environmental temperature
\dot{Q}_c	Thermal power transferred by convection
\dot{q}_c	Convection flux between surface and environment

h_c	Convection coefficient
I_i	Incident solar radiation
I_b	Direct beam radiation
I_d	Diffuse sky radiation
I_g	Radiation reflected from the ground
ϑ	Angle where beam radiation affect a surface
F_{sh}	Fraction of surface currently in shadow from other surrounding geometry
F_{sk}	Fraction of the diffuse sky visible in this instant from a surface

Table 10: Symbols and acronyms

553

554

Accepted Manuscript

555 Bibliography

- 556 Ambrosini R., Grueff G., Morsiani M., Maccaferri G., Zacchiroli P., Orfei A., Analysis of the alidade
557 temperature behaviour of the Medicina VLBI radiotelescope, *Astrophysics and Space Science*, 239, 247-
558 258, 1996.
- 559 Baars, J. W. The paraboloidal reflector antenna in radio astronomy and communication (Vol. 348). New York:
560 Springer, 2007.
- 561 Bhumralkar C. M., Numerical experiments on the computation of ground surface temperature in an
562 atmospheric general circulation model, *Journal of Applied Meteorology*, 14, 1246-1258, 1975.
- 563 Bolli P., Orlati A., Stringhetti L., Orfei A., Righini S., Ambrosini R., Bartolini M., Bortolotti C., Buffa F.,
564 Buttu M., Cattani A., D'Amico N., Deiana G., Fara A., Fiocchi F., Gaudiomonte F., Maccaferri A., Mariotti
565 S., Marongiu P., Melis A., Migoni C., Morsiani M., Nanni M., Nasyr F., Pellizzoni A., Pisanu T., Poloni
566 M., Poppi S., Porceddu I., Prandoni I., Roda J., Roma M., Scalambra A., Serra G., Trois A., Valente G.,
567 Vargiu G. P., Zacchiroli G., Sardinia Radio Telescope: General description, technical commissioning and
568 first light. *Journal of Astronomical Instrumentation*, 4(03n04), 1550008, 2015.
- 569 Buffa F., Causin A., Cazzani A., Poppi S., Sanna G., Solci M., Stochino F., Turco E., The Sardinia Radio
570 Telescope: A comparison between close-range photogrammetry and finite element models, *Mathematics
571 and Mechanics of Solids*, 22, 1005-1026, 2017.
- 572 Chen D., Xu W., Qian H., Sun J., Li J., Effects of non-uniform temperature on closure construction of spatial
573 truss structure, *Journal of Building Engineering*, 32, 101532, 2020.
- 574 Chen D., Xu W., Qian H., Wang H., Thermal behavior of beam string structure: Experimental study and
575 numerical analysis, *Journal of Building Engineering*, 40, 102724, 2021.
- 576 Drozdol K., CFD thermal analysis of a three-layer chimney used in residential buildings, *Journal of Building
577 Engineering*, 44, 102665, 2021.
- 578 Fu L., B. Ling Q. B., Geng X. G., Wang J. Q., Jiang Y. B., Yu L. F., Zhang Y. F., The alidade temperature
579 behaviour of TM65m antenna and its effects on pointing accuracy, *Advances in Optical and Mechanical
580 Technologies for Telescopes and Instrumentation II, Proc. SPIE 9912*, 99124J, 2016.

581 Greve A., Bremer M., Peñalver J., Raffin P., Morris D., Improvement of the IRAM 30-m Telescope from
582 temperature measurements and Finite-Element calculations, *IEEE Transactions on Antennas and*
583 *Propagation*, 53, 851-860, 2005.

584 Govoni F., Bolli P., Buffa F., Caito L., Carretti E., Comoretto G., Fierro D., Melis A., Murgia M., Navarrini
585 A., Orfei A., Orlati A., Pisanu T., Poppi S., Possenti A., Attoli A., Becciani U., Belli C., Carboni G., Caria
586 T., Cattani, A., Concu, R., Cresci L., Fara A., Fiocchi F., Gaudiomonte F., Ladu A., Maccaferri A., Mariotti
587 S., Marongiu P., Migoni C., Molinari E., Morisani M., Nesti R., Olmi L., Porceddu I., Righini S., Ortu P.,
588 Palmas S., Pili M., Poddighe A., Poloni M., Roda J., Scalambra A., Schillirò F., Schirru L., Serra G.,
589 Smareglia R., Vargiu G.P., Vitello F., The high-frequency upgrade of the Sardinia Radio Telescope. In
590 XXXIVth General Assembly and Scientific Symposium of the International Union of Radio Science (URSI
591 GASS) (pp. 1-4). IEEE, 2021.

592 Höpfe P. R., Heat balance modelling, *Experientia*, 49, 741-746, 1993.

593 Khemlani, L. Autodesk Revit: implementation in practice. White paper, Autodesk, 2004.

594 Kosky P., Balmer R., Keat W., Wise G., Exploring Engineering 3rd edition, *Academic Press*, 2013.

595 Li L., Lin W., Zhang T., Liu X., On-site measurement of thermal environment and heat transfer analysis in a
596 curling arena, *Journal of Building Engineering*, 34, 101691, 2021.

597 Losi G., Bonzanini A., Aquino A., Poesio P., Analysis of thermal comfort in a football stadium designed for
598 hot and humid climates by CFD, *Journal of Building Engineering*, 33, 101599, 2021.

599 Pisanu T., Buffa F., Poppi S., Marongiu P., Serra G., Vargiu G. P., Concu R., The SRT inclinometer for
600 monitoring the rail and the thermal gradient effects on the alidade structure, *Ground-based and Airborne*
601 *Telescopes V, Proc. SPIE 9145*, 91454R, 2014.

602 Prado R. T. A., Ferreira F. L. Measurement of albedo and analysis of its influence the surface temperature of
603 building roof materials, *Energy and Buildings*, 37, 295-300, 2005.

604 Stochino F., Cazzani A., Poppi S., Turco E., Sardinia Radio Telescope finite element model updating by means
605 of photogrammetric measurements, *Mathematics and Mechanics of Solids*, 22, 885-901, 2017.

- 606 Stolarski, T., Nakasone, Y., Yoshimoto, S. Engineering analysis with ANSYS software. Butterworth-
607 Heinemann, 2018.
- 608 Süß, M., Koch, D., Paluszek, H. The sardinia radio telescope (SRT) optical alignment. In Ground-based and
609 Airborne Telescopes IV (Vol. 8444, p. 84442G). International Society for Optics and Photonics (2012,
610 September).
- 611 Ukita N., Ezawa H., Ikenoue B., Saito M., Thermal and wind effects on the azimuth axis tilt of the ASTE 10-
612 m Antenna, *Publications of the National Astronomical Observatory of Japan*, 10, 25-33, 2007.
- 613 Vox G., Maneta A., Schettini E., Evaluation of the radiometric properties of roofing materials for livestock
614 buildings and their effect on the surface temperature, *Biosystems Engineering*, 144, 26-37, 2016.
- 615 Wang M., Ou T., Xin Z., Wang D., Zhang Y., Mechanical behavior and fatigue failure analysis of standing
616 seam aluminum alloy roof system under temperature effect, *Journal of Building Engineering*, 44, 103001,
617 2021.
- 618 Zhao Y., Du J., Xu Q., Bao H., Real-time monitoring of the position and orientation of a radio telescope sub-
619 reflector with fiber bragg grating sensors, *Sensors*, 19, 619, 2019.